www.sciencemag.org/content/351/6278/aad2001/suppl/DC1

Supplementary Materials for

Architecture of the type IVa pilus machine

Yi-Wei Chang, Lee A. Rettberg, Anke Treuner-Lange, Janet Iwasa, Lotte Søgaard-Andersen, Grant J. Jensen*

*Corresponding author. E-mail: jensen@caltech.edu

Published 11 March 2016, *Science* **351**, aad2001 (2016)
DOI: 10.1126/science.aad2001

This PDF file includes:

Other supplementary material for this manuscript includes the following:

Movies S1 to S3

Materials and Methods

Cell growth, generation of mutants and motility assays

M. xanthus strains used in this study are listed in Table S2 and are all derivatives of the wild-type strain DK1622 (*59*). *M. xanthus* strains were grown at 32 °C in CTT medium or on 1% CTT 1.5% agar plates supplemented with kanamycin (40 μg/ml) (*60*). Plasmids and primers are listed in Tables S3 and S4, respectively. In-frame deletions were generated as described (*61*). T4P-dependent motility was assayed as described (*62*). Briefly, exponentially growing cells were harvested and 5 μl aliquots were spotted at a cell density of 7×10^9 cells/ml on 0.5% agar supplemented with 0.5% CTT and incubated at 32 °C for 24 h. Colony edges were documented using a Leica MZ75 stereomicroscope equipped with a Leica DFC280 camera. Plasmids were propagated in *E. coli* TOP10 (F-, *mcrA*, Δ(*mrr-hsd*RMS-*mcr*BC), ϕ80*lac*ZΔM15, Δ*lac*X74, *deo*R, *rec*A1, *ara*D139, Δ(*ara, leu*) 7679, *gal*U, *gal*K*, rps*L, *end*A1, *nup*G) grown in LB broth.

Immunoblot analysis

For immunoblot analysis, cells from exponentially growing cultures were harvested and resuspended in SDS lysis buffer, and proteins from 3×10^8 cells were separated by SDS-PAGE. Immunoblotting was done using standard procedures using rabbit polyclonal antibodies against PilA (*63*), PilT (*64*), PilB (*64*), PilC (*22*), PilM (*22*), PilQ (*22*), PilN (*21*), PilO (*21*), PilP (*21*), and TsaP (*17*) in combination with secondary anti-rabbit immunoglobulin G peroxidase conjugate (Sigma). Blots were developed using Luminata Western HRP Substrate (Merck Millipore).

T4P shearing assay

T4P were sheared from cells that had been grown on 1% CTT 1.5% agar plates at 32°C for 2-3 days and analyzed by immunoblot with anti-PilA antibodies as described (*65*).

Identification of minor pilins

The minor pilins of *P. aeruginosa* (FimU, PilV, PilW, PilX and PilE) and *N. meningitidis* (NMB0886-0889, 2016 and 0547) belong to five clusters of orthologous proteins (COGs) (*66*). Using the COG database (http://www.ncbi.nlm.nih.gov/COG/) and a COG Guess search (http://www-archbac.u-psud.fr/genomics/COG_Guess.html) we found that (i) MXAN0359, MXAN1017, MXAN1369 and MXAN2506 belong to COG4970 with FimU; however, MXAN2506 is annotated as *gspJ* and is part of the T2SS-encoding locus of *M. xanthus* (*67*). (ii) MXAN0361, MXAN1019, MXAN1368 and MXAN2507 belong to COG4967 with PilV; however, MXAN2507 is annotated as *gspI* and is part the T2SS-encoding locus of *M. xanthus*. (iii) MXAN0360, MXAN1018 and MXAN1367 belong to COG4966 with PilW. (iv) MXAN0364 belongs to COG4726 with PilX. No PilE orthologs were identified. BlastP searches of the *M. xanthus* genome using the identified minor pilins as seeds did not identify additional minor pilins except for the minor pseudopilins encoded by the T2SS locus. Accordingly, we named MXAN0359-0361 and MXAN0364 *fimU1*, *pilW1*, *pilV1* and *pilX1*; MXAN1017-1019 *fimU2*, *pilW2* and *pilV2*; and MXAN1367-1369 *pilW3*, *pilV3* and *fimU3* (Fig. S5A).

Electron cryotomography

M. xanthus cells were grown to an OD_{550nm} of 0.8. 10-nm colloidal gold (Sigma-Aldrich, St. Louis, MO) pretreated with bovine serum albumin was added to the cells to serve as fiducial markers during tomogram reconstruction. 3 µl of the resulting sample was pipetted onto a freshly glow-discharged Quantifoil copper R2/2 200 EM grid (Quantifoil Micro Tools GmbH, Jena, Germany) and plunge-frozen in a liquid ethane propane mixture using an FEI Vitrobot mark-III (FEI Company, Hillsboro, OR). The frozen grids were then imaged in an FEI Tecnai G2 Polara 300 keV field emission transmission electron microscope (FEI Company, Hillsboro, OR) at the California Institute of Technology or an FEI Titan Krios (FEI Company, Hillsboro, OR) at the Howard Hughes Medical Institute Janelia Research Campus. Both electron microscopes are equipped with a Gatan energy filter (Gatan, Pleasanton, CA) and a Gatan K2 Summit direct detector (Gatan, Pleasanton, CA). Energy-filtered tilt series of images of cell poles were collected automatically from −60° to +60° at 1° intervals using the UCSF Tomography data collection software (*68*) with total dosage of 150 $e^-/Å^2$, a defocus of -6 µm and a pixel size of 3.9 Å. The images were aligned and contrast transfer function corrected using IMOD software package (*69*). SIRT reconstructions were then produced using the TOMO3D program (*70*). T4PM basal body structures on cell envelopes were located by visual inspection. Sub-tomogram averages with 2-fold symmetrization along the particle Y-axis were produced using the PEET program (*71*). Central slices of the sub-tomogram averages were rotated along the particle Y-axis to generate 3-D molecular envelopes.

Identification of empty basal bodies

Piliated T4PMs were easily recognized on the cell surface through their 6-nm diameter pili (Fig. 1B, white arrows). T4PM basal bodies exhibited three layers of densities in the periplasm and a fourth in the cytoplasm (Fig. 1C). In the vicinity of piliated T4PMs, we also observed structures with three similar periplasmic layers but without long fibers attached (Fig. 1B, black arrow and Fig. 1D). Due to their remarkably similar appearance and location, we hypothesized that these structures were empty (non-piliated) T4PM basal bodies. Several lines of evidence support that these structures represent T4PM basal bodies. First, *M. xanthus* cells only assemble T4P at one pole at a time (*59*); however, occasionally cells reverse their direction of movement and in parallel with a reversal the pole at which T4P assemble changes (*72*). Consistent with previous reports showing that preassembled T4PM are present at both poles (*17*, *21*, *22*), we only observed T4P at one of the cell poles while putative empty basal bodies were observed at both cell poles. Second, neither piliated nor the putative empty basal bodies were found in tomograms of a Δ*pilQ* mutant (Table S1) that lacks PilQ, which functions as the initiating platform for T4PM assembly in *M. xanthus* (*21*). Third, only putative empty basal bodies were observed in the Δ*pilA* mutant that lacks the pilin subunit PilA (Table S1). Fourth, mutants lacking PilB (which cannot assemble T4P) or PilT (which cannot retract T4P) only contained putative empty basal bodies and piliated basal bodies, respectively (Table S1).

Higher resolution of Δ*pilB* structure

In the Δ*pilB* mutant (Fig. 2J2), we found that although the empty basal body has an overall conformation nearly identical to that of wild-type, better local resolutions were achieved on the IM-associated parts (Fig. S1A, C). Clearer connections between the lower-periplasmic ring and the IM could be resolved, and the density of the cytoplasmic ring was stronger. One possible reason for this improved resolution may be that every particle was stalled in a "pilus-preassembly" state to which PilT cannot bind. In contrast, the empty basal bodies captured in wild-type cells might reflect additional stages either before pilus assembly or after pilus disassembly. This observation suggests that while PilB and PilT occupy the same basic location, their binding and release do at least subtly perturb the cytoplasmic ring and the connections between the lower-periplasmic ring and the IM.

Modeling the empty T4PM basal body

Because atomic structures are available for homologs of >90% of the domains of the T4PM, to test the plausibility of our component maps we explored models of the T4PM that matched the EM density and agreed with all known component sizes, interfaces and connectivities (see Movie 1 for a presentation of the following in 3-D). The description starts with the empty basal body, followed by the piliated form.

- *PilQ and PilP*

M. xanthus PilQ is composed of three β-domains in the N-terminal region, followed by the two homologous N0 and N1 domains, and a C-terminal transmembrane secretin domain. Recent single particle reconstructions of purified secretin domains of *Klebsiella oxytoca* T2SS PulD (*44*) (homologous to T4PM PilQ) revealed a structure containing a plug (gate) and periplasmic vestibule similar to those of the OM pore in our empty T4PM basal body structure (Fig. S4). By aligning these structures, we determined that the secretin domain forms the OM pore and extends all the way to the mid-periplasmic ring but is not part of it. We also observed a movement of the OM pore farther away from the mid-periplasmic ring in the piliated state (Fig. 2B3 and Movie S3). We find that the new space appears just where the secretin domain ends (Fig. S4), so it must involve restructuring of the N1 domain or the connection between secretin and N1 domains. This agrees with the previous observation that purified secretin domains with and without an N3 domain (corresponding to the N1 domain in *M. xanthus* T4PM) result in very similar reconstructions (*44*) (Fig. S4), likely due to a dynamic or unstructured N3 domain. In these reconstructions, however, as discussed in the main text, the shape and length of the predicted transmembrane region of the purified secretin domain do not match our in vivo structure. A similar discrepancy in particle length between in vivo and in vitro secretin-containing molecules has been observed for the T3SS (*73*). To produce a better representation of the secretin domain structure in vivo, we took advantage of the Δ*tsaP* empty basal body structure (Figs. 2D3 and S4A), which has no TsaP and also exhibits the disengaged conformation, revealing the in vivo structure of the secretin domain alone (represented as a brown surface in Fig. S12B).

The PilP lipoprotein is composed of a long disordered periplasmic N-terminal region covalently linked to a lipid moiety in the IM and a C-terminal soluble homology region

(HR) domain. PilP uses its HR domain to interact with the N0 domain of PilQ (*25*). The crystal structures of the *P. aeruginosa* PilP HR domain (PDB 2LC4) (*28*) and the *N. meningitidis* PilQ N0 domain (PDB 4AR0) (*41*) have been solved individually. Using these structures as templates, and as for all other atomic models placed into the EM density maps, we first generated homology models of the *M. xanthus* structures ($PilP_{HR}$ and $PilQ_{N0}$) using the Phyre2 server (*74*). The protein sequence coverage of all models and their modeling confidence level reported are listed in Table S5. The crystal structure of the enterotoxigenic *Escherichia coli* T2SS GspC (homologous to PilP in T4PM) HR domain complexed with the N0 and N1 domains of GspD (homologous to PilQ N0 and N1 in T4PM) has also been solved (PDB 3OSS) (*32*). Superposing the $PilP_{HR}$ and $PilQ_{N0}$ models on the corresponding parts in the T2SS structure shows overall *root-mean-square deviation* of 1.2 Å and 1.7 Å, respectively, suggesting that PilP and PilQ in the T4PM likely use the same binding mode to form a complex (Fig. S7A, B). We then accordingly generated a homology model of the *M. xanthus* $PilP_{HR}$:$PilQ_{N0-N1}$ complex. PilQ homologues in different species have been reported to form channels with different oligomeric states including 12-, 14- and 15-mers (*33*, *41*, *42*, *44*, *50*, *75*, *76*). To investigate the oligomeric state of PilQ in *M. xanthus* T4PM, we generated different $PilP_{HR}$:$PilQ_{N0-N1}$ ring models using 12- to 15-fold symmetries with SymmDock (*77*) (a program that generates candidate multimeric ring models), and examined their fit within the mid-periplasmic ring envelope. After testing 50 different ring models of each fold symmetry, only one $PilP_{HR}$:$PilQ_{N0-N1}$ ring matched the size of the ring and satisfied both constraints that PilP resides on the periphery of the ring (Fig. 2C1-C5) and the PilQ N1 domains reside in the constriction of the periplasmic vestibule structure connecting to the secretin domain (Fig. S7C). Because this model was a 12-mer, we proceeded with the assumption that the PilQ channel is dodecameric in *M. xanthus*. Sequence-based secondary structure prediction and intrinsic disorder prediction suggested that PilP N-terminal region lacks regular secondary structure (*28*). The N-terminal region was then modeled as a disordered random coil to connect the HR domain to the IM (see below).

The PilQ N-terminal β1-domain (Fig. S4B) was predicted to be an amidase N-terminal (AMIN) domain, a reported PG binding domain with a solved crystal structure (*78*). Because the β2-domain's predicted secondary structure is the same (data not shown), it is likely a repeat of the AMIN domain. The structure of the β3-domain has also been solved (*41*), showing similar folding to that of AMIN domains. These three AMIN domains are connected by unstructured linkers. Because there was no clear density left in the average map for assigning the 36 AMIN domains from a dodecameric PilQ complex, we hypothesize that they bind to PG irregularly, causing their densities to be unresolved in the sub-tomogram averages. To test this hypothesis, we imaged a *pilQ* mutant in which the first and second AMIN domains (corresponding to amino acid residues 25-300) had been deleted ($\Delta pilQ_{\beta1\text{-}\beta2}$). The generated sub-tomogram averages of piliated and empty T4PM basal bodies show no clear difference to those of wild-type cells (Fig. S8A, B), supporting our assignment. Interestingly, even though the $\Delta pilQ_{\beta1\text{-}\beta2}$ mutant fully assembled T4PM, it displayed a reduced number of pili compared to wild-type (Table S1). Consistently, T4P-dependent motility was reduced (Fig. S8C). This observation is consistent with a previous study in *P. aeruginosa* showing that removal of the PilQ N-terminus up to the N0 domain did not disrupt secretin channel formation but significantly

reduced motility (*79*). To further display the possible arrangement of the 36 AMIN domains on the PG surrounding the T4PM basal body, we first generated models of the first and second AMIN domains based on the crystal structure an *E. coli* N-acetylmuramoyl-L-alanine amidase AmiC AMIN domain (PDB 4BIN) (*78*), and a model of the third AMIN domain based on the structure of a *N. meningitidis* PilQ β2 domain (PDB 4AQZ) (*41*). The models were then placed randomly on the PG constrained by their known linker lengths. As shown in Figure 3D the random configuration of the AMIN domains is not expected to generate a well-defined density in the sub-tomogram averages.

- *TsaP*

A previous report has shown that TsaP binds to PG and associates with the OM in a PilQ-dependent manner (*17*). TsaP was therefore proposed to link the PilQ channel to the PG. TsaP contains an N-terminal carbohydrate-binding lysine motif (LysM) domain and a C-terminal domain with unknown function. Using the Phyre2 server, the TsaP C-terminal domain was predicted to be a structural homologue of the C-terminal domain of flagellar motor component FlgT, which forms a ring structure on the periphery of the flagellar basal body close to the OM in the periplasm and is involved in anchoring the flagellar base to the cell surface (*80*, *81*). Here, the missing ring-like peripheral density on the PilQ channel in the Δ*tsaP* mutant (Fig. 2D2, D4) suggests a similar configuration of TsaP in the T4PM basal body. By sub-tomogram averaging random volumes spanning the *M. xanthus* cell envelope, we were able to detect the average position of the PG layer in the periplasm, and introduce its structure at the correct level in the overall T4PM models (Fig. S12). The missing densities in the piliated and empty basal body of the Δ*tsaP* mutant are more than 7 nm and 5 nm away from the PG, respectively. We suggest that TsaP exhibits a dynamic elongated conformation, using its C-terminal FlgT-homologous domain to interact with the PilQ channel at a position immediately below the OM, and using a flexible linker region to extend its LysM domain for binding to the PG. As for the β-domains of PilQ, the flexibility of this linker region likely prevents the visualization of the linker and the LysM domain in the sub-tomogram averages. Homology models of the *M. xanthus* TsaP N- and C-terminal domains were generated based on the structures of a *Magnaporthe oryzae* lectin LysM domain (PDB 2L9Y) (*82*) and a *Vibrio alginolyticus* FlgT protein (PDB 3W1E) (*83*), respectively. Using the SymmDock software, we were able to generate a dodecameric ring model of the TsaP C-terminal domain that fits the density well (Fig. S7D). We then placed 12 LysM domain models on top of the PG layer to represent the overall TsaP configuration in the basal body (Fig. S12B).

- *PilO and PilN*

The bitopic IM proteins PilN and PilO are structural homologues, composed of a short cytoplasmic N-terminus followed by a single transmembrane segment, an α-helix predicted as a coiled-coil domain, and a C-terminal globular domain in the periplasm (*23*, *27*). Previous studies have shown that isolated PilO forms homodimers in solution, but switch entirely to stable heterodimers with PilN when mixed together (*30*), suggesting that PilO homodimers and PilN:PilO heterodimers share the same protein-protein interface, with higher affinity for heterodimer formation. An in vivo disulfide-bond cross-

linking assay has also suggested that the PilN and PilO homologues in the T2SS use the same protein-protein interface to form both homodimers and heterodimers (*84*). Finally, since only heterodimers of PilN and PilO are able to interact with PilP (*28*), and these three proteins mutually stabilize each other in *M. xanthus* (*21*), the PilN and PilO in T4PM are likely heterodimeric. Unfortunately, so far only homodimeric crystal structures of PilN from *T. thermophilus* (PDB 4BHQ) (*33*) and PilO from *P. aeruginosa* (PDB 2RJZ) (*30*) have been solved. In these structures, the same surface used to form homodimers of PilO produces tight crystal packing of PilN (Fig. S9A). This interface matches the previous in vivo disulfide-bond cross-linking results (*84*). We therefore used this interface to generate a PilN:PilO heterodimer by swapping a subunit in the PilN homodimer to PilO (Fig. S9A). We removed the N-terminal α-helices of both the PilN and PilO structures, since they are truncated coiled-coils that folded into the homodimer interfaces and might have different orientations under physiological conditions. Based on the direct binding of PilQ to PilP, PilP to the PilN:PilO heterodimer, and PilN to PilM, the stoichiometry of PilM:PilN:PilO:PilP:PilQ is likely 1:1:1:1:1. Accordingly, proteins in the alignment complex all likely form dodecameric complexes in the basal body, as determined for PilQ. We therefore used SymmDock to generate 12-mer rings of the heterodimeric PilN:PilO globular domain models to occupy the lower-periplasmic ring of the empty basal body envelope (Fig. S9B). The result with the best fit exhibited an overall configuration of a 12-mer PilN ring stacked on a 12-mer PilO ring, with the PilN ring located farther from the IM. Next, in the thin densities connecting the lower-periplasmic ring to the IM, we modeled a long coiled-coil structure using the sequences of the remaining N-terminal portions of PilN and PilO. Interestingly, the longer remaining N-terminal region of PilN (111 residues) relative to PilO (87 residues) (Fig. S9A) positioned the transmembrane segments of both proteins nicely right in the hydrophobic core of the IM. This match between the length of the coiled-coil domain and the distance from the lower-periplasmic ring to the IM strongly supports our positioning of PilN and PilO. Subsequently, since the PilP disordered N-terminal region interacts with the PilN:PilO complex (*28*), we modeled the PilP disordered part adjacent to PilN:PilO to allow direct interactions (Fig. S12B). Together, the dodecameric PilN:PilO resembles a ring suspended in the periplasm, anchored in the IM by 12 elongated coiled-coil structures and linked to the OM pore complex through the disordered N-terminal regions in the 12 PilP molecules.

- *PilM*

PilM is a cytoplasmic protein possessing an actin-like fold. A crystal structure of PilM complexed with ATP and a short N-terminal peptide of PilN ($PilN_{N\text{-}terminus}$) from *T. thermophilus* has been reported (PDB 2YCH) (*31*). To place the PilM structure into the cytoplasmic ring density of the empty basal body, we first used SymmDock to generate different ring structures containing 12 PilM:$PilN_{N\text{-}terminus}$ complexes. We then selected the ring whose diameter best matched our EM measurements, and in which the bound $PilN_{N\text{-}terminus}$ peptides faced the IM when placed into the cytoplasmic ring (Fig. S9C). Remarkably, in this model, the $PilN_{N\text{-}terminus}$ peptides complexed with PilM were well positioned to connect with the N-termini of the previously-modeled PilN transmembrane segments supporting the proposed structure of the dodecameric PilM:$PilN_{N\text{-}terminus}$ ring. Notably, after connecting PilM to the PilN:PilO lower-periplasmic ring, the height of this

IM-crossing complex was much larger than in previously reported single particle reconstructions (*33*) (Fig. S14), likely due to loss and collapse of the elongated PilN:PilO coiled-coil structures upon purification.

- *PilA* and *minor pilins*

The four minor pseudopilins (GspH, GspI, GspJ, and GspK) in the T2SS are thought to form a complex that primes pseudopilus formation by the major pseudopilin (GspG) (*47*, *48*). Similarly, the minor pilins in the T4PM are thought to form a complex that primes pilus formation by the major pilin PilA (*46*). However, the precise composition of this complex in the T4PM is not known. Based on crystal structures and cryo-EM data, an atomic model of the T4P fiber has been described (PDB 2HIL) (*18*). In this model, the N-terminal α-helices of the major pilin subunits are bundled in a helical manner, forming the core of the pilus fiber, and positioning the C-terminal globular domains on the pilus surface. Based on this model, pilins assemble into a right-handed helix with 6 nm diameter, 3.6 subunits per turn and 3.7 nm pitch. The main stabilizing force in the pilus is the formation of a 3-helix bundle of the N-terminal hydrophobic α-helices of pilin subunits N, N+3 and N+4. The minor pseudopilins GspI, GspJ, and GspK from the T2SS in enterotoxigenic *E. coli* form a 1:1:1 complex and have been suggested to arrange together with GspH and GspG into a quasihelical structure similar to the helical structure formed by the major pilin in the T4PM (*85*). Due to the lack of structural information of T4PM minor pilins, we generated a model of the short stem in the empty basal body by five PilA major pilin subunits in a helical arrangement (Fig. S12B). This structure is not only the shortest PilA helix predicted to be stable but also matches the short stem density well.

- *PilC*

PilC is a polytopic IM protein containing an N-terminal globular domain ($PilC_N$), a central transmembrane part, a C-terminal globular domain ($PilC_C$), and another C-terminal transmembrane segment (Fig. S10A). Different studies of PilC homologues have proposed either two or three transmembrane segments in the central part of the protein, resulting in discrepancies in PilC topology, with either the two globular domains both located in the cytoplasm (*86*, *87*) or one on each side of the IM (*88*). In recent studies, it was suggested that $PilC_N$ and $PilC_C$ interact with the ATPases PilB and PilT, respectively (*49*), suggesting that both domains are cytoplasmic. Moreover, here we did not observe additional densities on the periplasmic face of the IM beyond what would be needed for the 5-PilA pilus stem (as a proxy for the PilA/minor pilin structure), but we did detect a distinct dome on the cytoplasmic side of the IM. We therefore hypothesize that both PilC globular domains are located in the cytoplasm.

To date, crystal structures of the $PilC_N$ from *T. thermophilu*s ($TtPilC_N$, PDB 2WHN) (*34*) and its homologues EpsF N-terminal domain from *V. cholerae* T2SS ($VcEpsF_N$, PDB 3C1Q) (*35*) and the TcpE N-terminal domain from *V. cholerae* toxin-coregulated pilus ($VcTcpE_N$, PDB 4HHX) (*89*) have been solved. While the $PilC_C$ exhibits significant sequence identity with, and is considered a structural repeat of, the $PilC_N$, no structure of the $PilC_C$ has been solved. Nor has there been solved a structure of the transmembrane regions. Interestingly, even though both of the $TtPilC_N$ and $VcEpsF_N$ structures formed

dimers in crystals, they used completely different dimerization interfaces, whereas $VcTcpE_N$ remained monomeric. Full-length PilC was reported to form predominantly dimers in solution, and the previously reported single particle EM density of a purified *N. meningitidis* PilG tetramer (*90*) (homologous to *M. xanthus* T4PM PilC) is significantly larger than the cytoplasmic dome density and would sterically clash with the cytoplasmic disc density of the PilB/PilT ATPases in the piliated T4PM basal body (Fig. S10D). We therefore propose that PilC forms a dimer under physiological condition in the T4PM. To examine the plausibility of the cytoplasmic dome being a PilC dimer by fitting its model, we first produced homology models of the *M. xanthus* $PilC_N$ and $PilC_C$ domains based on the structures of $VcEpsF_N$ and $TtPilC_N$, respectively, according to the top ranked results from the Phyre2 server. We then hypothesized that one of the reported dimerization interfaces mediates dimerization of PilC, and the other mediates association of the $PilC_N$ and $PilC_C$ domains, and generated a full-length PilC dimer model by: (i) swapping one subunit of the $PilC_N$ dimer model by a $PilC_C$ to generate a model of $PilC_{N,C}$; (ii) associating two $PilC_{N,C}$ at their C-terminal domains based on the dimerization model of $TtPilC_N$; (iii) connecting the $PilC_N$ and $PilC_C$ domains by two antiparallel transmembrane α-helices; (iv) adding the C-terminal transmembrane α-helix (Fig. S10B). The resulting model of full-length PilC dimer exhibited an elliptical cross-section of the cytoplasmic domains sufficient to fill the cytoplasmic dome density (Fig. S10C). Intriguingly, the model of the full-length PilC dimer exhibits an asymmetrical dimeric structure due to the asymmetrical dimerization mode reported for the $TtPilC_N$. In order to allow the two $PilC_N$ or $PilC_C$ domains in the PilC dimer to interact equally with ATPases held parallel to the IM by the PilM ring (see below), the transmembrane segments of PilC in the IM would form a tilted "glove" within the IM (Fig. S10E). Since PilC has been shown to interact with the N-terminus of PilA (*23*), this structural hypothesis suggests interesting possibilities about how it interacts with pilins and the pilus to cause extension and retraction (see Discussion).

Modeling the piliated T4PM basal body

- *PilM*

The most obvious differences between the piliated and non-piliated EM density maps are the presence of an extended pilus and a cytoplasmic disc. Upon careful inspection one sees that the cytoplasmic ring is also larger in diameter (Fig. 1E-H). A new dodecameric PilM:$PilN_{N\text{-terminus}}$ ring was therefore chosen from 50 SymmDock candidates (Fig. S9D) that matched the new ring dimension, pointed the $PilN_{N\text{-terminus}}$ peptide towards the IM, and exposed the conserved surface for binding the assembly ATPase PilB (see below) (Fig. S11A, B). Interestingly, in the new ring the $PilN_{N\text{-terminus}}$ peptides emerged farther away from the T4PM axis (Fig. S12, blue stars). We therefore remodeled the PilN:PilO coiled-coil structures slightly to reach the new position of the $PilN_{N\text{-terminus}}$ peptides, and as a result the gaps between each PilN:PilO coiled-coil structure widened (Fig. S12A). A crystal structure of the T2SS EpsL cytoplasmic domain (homologous to T4PM PilM) complexed with the EpsE (homologous to T4PM PilB) N-terminal domain has been solved (PDB 2BH1) (*36*). Even though a bacterial two-hybrid assay did not detect interaction between PilM and PilB homologues from *N. meningitidis* (*23*), the structurally conserved EpsE:EpsL interface on PilM allowed us to propose a putative PilB binding surface on PilM (Fig. S11A). We found that in our cytoplasmic ring

models, the proposed PilB binding site on PilM was buried in the non-piliated state, but fully exposed in the piliated state (Fig. S11B). This observation suggests that the cytoplasmic ring could modulate ATPase binding through a conformational shift.

- *PilB and PilT*

Both PilB and PilT belong to the secretion ATPase family and are composed of an N-terminal domain (NTD) followed by a flexible linker connecting to a C-terminal ATP-binding domain (CTD). Crystal structures of *Archaeoglobus fulgidus* GspE (homologous to T4PM PilB, PDB 2OAQ) (*37*) and *P. aeruginosa* PilT (PDB 3JVV) (*38*) have revealed their hexameric configurations and ATP-hydrolysis driven conformational changes. During ATP binding and hydrolysis, the CTDs in the hexamers remain relatively fixed while the NTDs move using the flexible linkers as hinges. These ATP-hydrolysis-coupled domain movements must ultimately be the force that drives the motor complex to assemble/disassemble the pilus. Moreover, NTD is responsible for correct polar localization of PilT in *P. aeruginosa* (*91*), suggesting its role of bridging PilT with other T4PM components in the IM. We therefore generated and placed ATPase hexamer models into the cytoplasmic disc density with the NTDs facing the IM. The best-fitting PilM ring model and our placement of the PilB hexamer within that ring reassuringly reproduced the PilB:PilM binding interface seen in the complex crystal structure of their T2SS homologues described above (PDB 2BH1) (*36*). In this ring model, the NTDs in the PilB hexamer interact with every second PilM in the dodecameric PilM ring. Interestingly, even though both ATPase hexamers exhibit a bowl-like overall shape, PilB's N-terminal region is significantly wider than PilT's (Fig. S10E). Since the modeled PilC dimer's cytoplasmic region has an elliptical cross-section with the C-terminal domains in the center and the N-terminal domains on the outside, this difference in ATPase shape would allow PilB and PilT to interact with the $PilC_N$ and $PilC_C$, respectively (Fig. S10E), just as suggested by previous studies (*49*), even though both are centered on the T4PM axis by the PilM ring.

- *PilN and PilO*

The only adjustment needed in the PilN and PilO model was a slight shift of the coiled-coils away from the T4P axis in order to reach the PilN binding site on the expanded PilM cytoplasmic ring (Fig. S11C and S12A). Interestingly, when the 12 PilN:PilO N-terminal coiled-coil structures are modeled into the density visible in the non-piliated empty state, the spaces between the coiled-coil structures in the periplasm are not wide enough for a PilA globular “head” domain to pass through (Fig. S11C, left). However, once the PilB hexamer binds and the PilN:PilO coiled-coil structures spread apart (Fig. S11C, right), the gaps between the PilN:PilO N-terminal coiled-coil structures in the enlarged dodecameric cage are big enough for PilA to enter and interact with PilC (Fig. 11C, right). Also, the EM data reveals that PilT-binding maintains the same enlarged PilM ring (Fig. 2J4), so pilin subunits would be able to diffuse away into the membrane during retraction. Finally, the shift of the PilN:PilO coiled-coils away from the T4P axis offers a possible explanation for why the connection density between the lower periplasmic ring and the IM appears weaker in the piliated structure (because the coiled-coils are spread farther apart and are also perhaps more mobile).

- *PilC and PilA*

No changes were necessary in the model of PilC, as it fit nicely in the pockets created by PilB and PilT, engaging the correct surfaces as described above. The previously reported atomic model of the pilus fiber (*18*) fit well into the stem density. Thirty-five PilA subunits of that model in total are shown in Figure S12A as a helical fiber extending from the PilC glove in the IM through the lower and mid-periplasmic rings and finally the OM pore.

- *PilQ, PilP and TsaP*

The last major difference between the piliated and empty T4PM structures is that the OM pore shifts up (distally) ~2 nm in the piliated structure, creating a gap between the secretin domain and the mid-periplasmic ring (Fig. 1E-H). The PilQ secretin domain surface and OM (bilayer) model were therefore shifted up to match the EM density map, and the gate region was removed to accommodate the extended pilus. No changes were made to the $PilQ_{N1,N0}$ and $PilP_{HR}$ domain models. The PilP N-terminal disordered regions were shifted slightly to remain next to the remodeled PilN:PilO coiled-coil structures. TsaP N- and C-terminal domains were placed on the PG and the periphery of PilQ, respectively, as in the empty basal body model, but with a more extended linker conformation as required by the OM pore shift

- *Combined structures*

Lastly, we combined these models of the different structural features of the piliated and non-piliated basal bodies to obtain hypothetical working models for the two states of the basal body (Fig. S12).

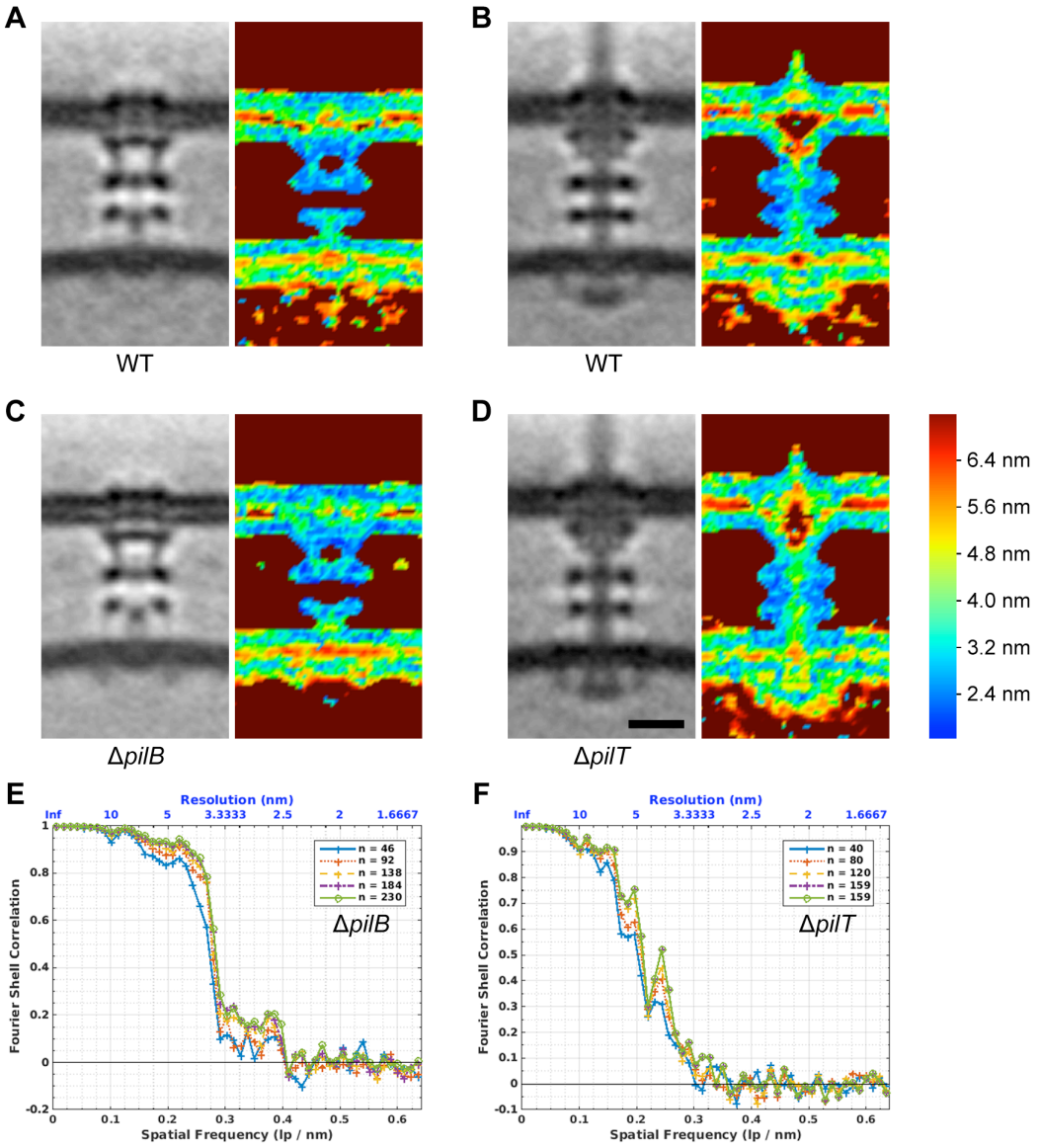

Fig. S1. Resolution of *M. xanthus* T4PM sub-tomogram averages. (**A**) Central slice through the sub-tomogram average of wild-type empty T4PM basal body (left) and local resolution estimated by Resmap (*92*) corresponding to the slice (right). (**B-D**) The same presentation as in (**A**) but of wild-type piliated (**B**), Δ*pilB* empty (**C**), and Δ*pilT* piliated (**D**) T4PM basal bodies. Scale bar in (**D**) 10 nm (applies to **A-D**). (**E**, **F**) Fourier shell correlation curves between maps calculated from half datasets of Δ*pilB* and Δ*pilT* sub-tomogram averages, respectively. Particle numbers used for generating each curve are indicated in the inset.

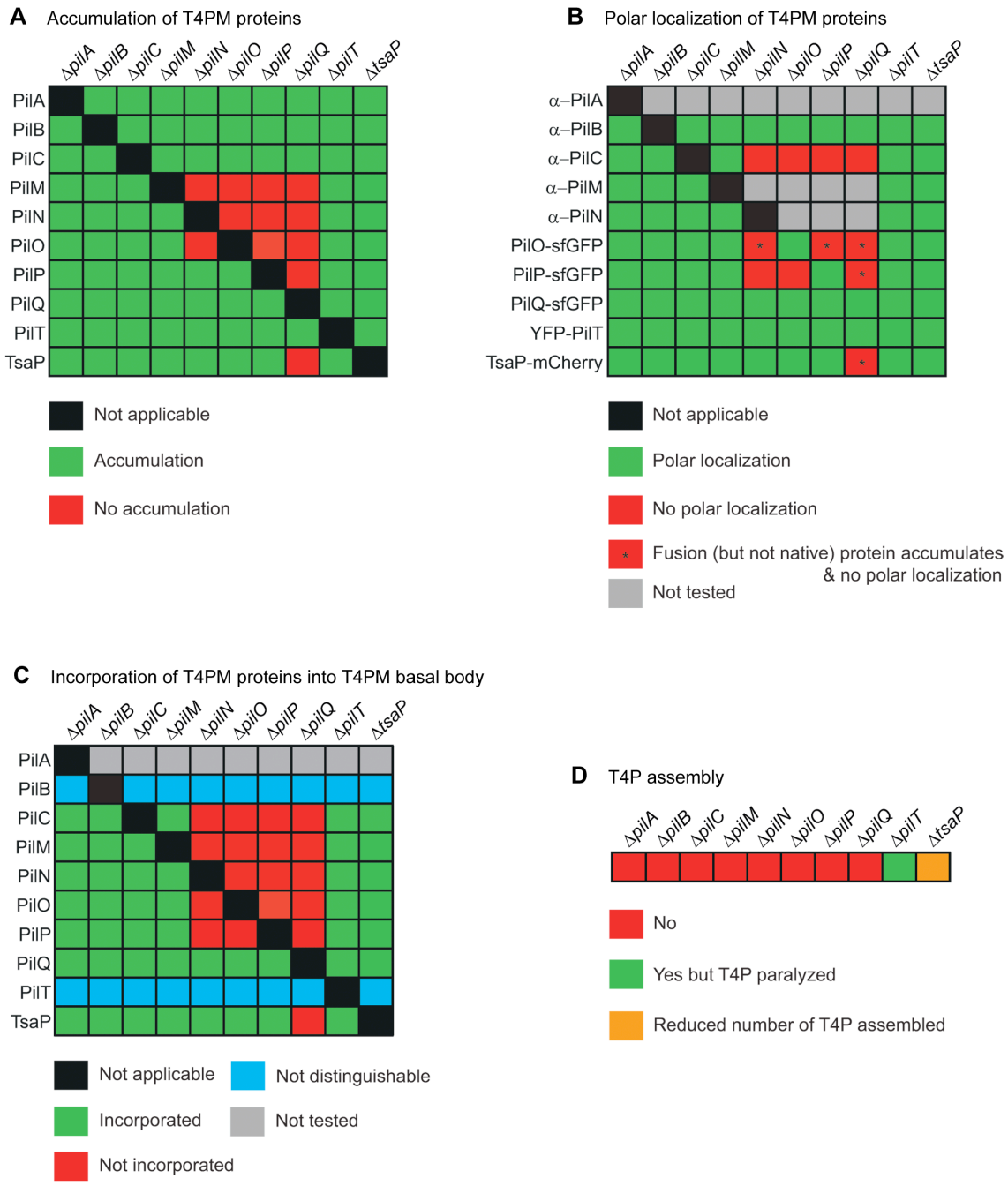

Fig. S2. Accumulation of T4PM proteins and their polar localization. (**A**) Panel summarizes the accumulation of T4PM proteins in the absence of each individual other T4PM protein (*17*, *21*). (**B**) Panel summarizes the polar localization pattern of T4PM proteins in the absence of each individual other T4PM protein as determined using immuno-fluorescence microscopy or active fluorescent fusion proteins (*17*, *21*, *22*). PilC, PilM, PilN, PilO, PilP, TsaP and PilQ localize at both cell poles whereas PilB and PilT are mostly unipolarly localized (*17*, *21*, *22*). All five fusion proteins are active and support the formation of functional T4P. Native PilP does not accumulate in the absence

of PilQ and native PilO does not accumulate in the absence of PilN, PilP or PilQ. However, the active fusion proteins (PilO-sfGFP and PilP-sfGFP) accumulate in these mutant backgrounds but do not localize to the cell poles. (**C**) Panel summarizes incorporation of T4PM proteins into the T4PM basal body in the absence of each individual other T4PM protein. With the exception of PilB and PilT (See below), polar localization of a protein is used as a readout for its incorporation into the T4PM (*17*, *21*). Specifically, PilC accumulates in the Δ*pilN*, Δ*pilO*, Δ*pilP* and Δ*pilQ* mutants (**A**) but is not polarly localized in these four mutants (**B**). Therefore, we deduce that PilC is not incorporated into the T4PM in these four mutants. PilM does not accumulate in the Δ*pilN*, Δ*pilO*, Δ*pilP* and Δ*pilQ* mutants (**A**) and therefore we deduce that PilM is not incorporated into the T4PM in these four mutants. PilN does not accumulate in the Δ*pilO*, Δ*pilP* and Δ*pilQ* mutants (**A**) and therefore we deduce that PilN is not incorporated into the T4PM in these three mutants. PilO does not accumulate in the Δ*pilN*, Δ*pilP* and Δ*pilQ* mutants (**A**) and therefore we deduce that PilO is not incorporated into the T4PM in these three mutants. Note that all these observations are consistent with and support the identification of the cytoplasmic ring as PilM, the cytoplasmic dome as PilC, and the lower periplasmic ring as PilN:PilO, as all of these are absent in the ΔpilP average (Fig. 2B1). Native PilP does not accumulate in the Δ*pilQ* mutant (**A**) whereas PilP-sfGFP does (**B**). However, PilP-sfGFP is not polarly localized in the Δ*pilN*, Δ*pilO*, and Δ*pilQ* mutants (**B**). Therefore, we deduce that PilP is not incorporated into the T4PM in these three mutants. TsaP does not accumulate in the Δ*pilQ* mutant (**A**) whereas TsaP-mCherry does (**B**). However, TsaP-mCherry is not polarly localized in the Δ*pilQ* mutant. Therefore, we deduce that TsaP is not incorporated into the T4PM in this mutant. In the case of PilB and PilT their mostly unipolar localization is independent of all other T4PM proteins (*21*, *22*) and depends on the small GTPase SofG and the bactofilin BacP (*93*) as well as the small GTPase MglA (*94*). Therefore, polar localization of PilB and PilT does not serve as a read-out for their incorporation into the T4PM basal body. (**D**) Panel summarizes T4P assembly in the absence of individual T4PM proteins (*21*, *22*, *45*, *95*, *96*).

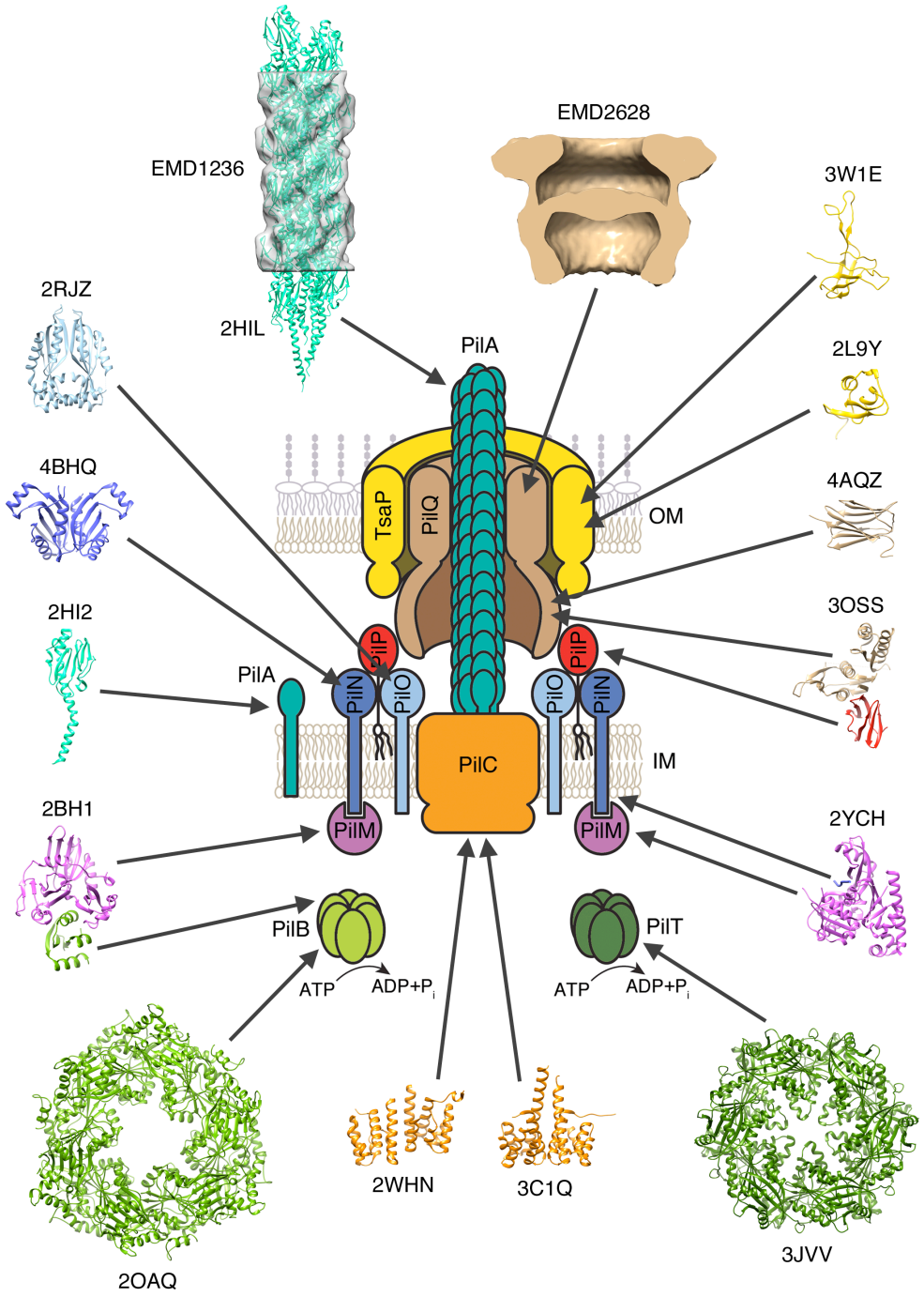

Fig. S3. Nomenclature, representative known homology structures, and prior knowledge of locations and interactions of *M. xanthus* T4PM subunits. Note that 2RJZ, 4BHQ, 2WHN, and 3C1Q crystal structures are homodimers; 2OAQ and 3JVV are hexamers.

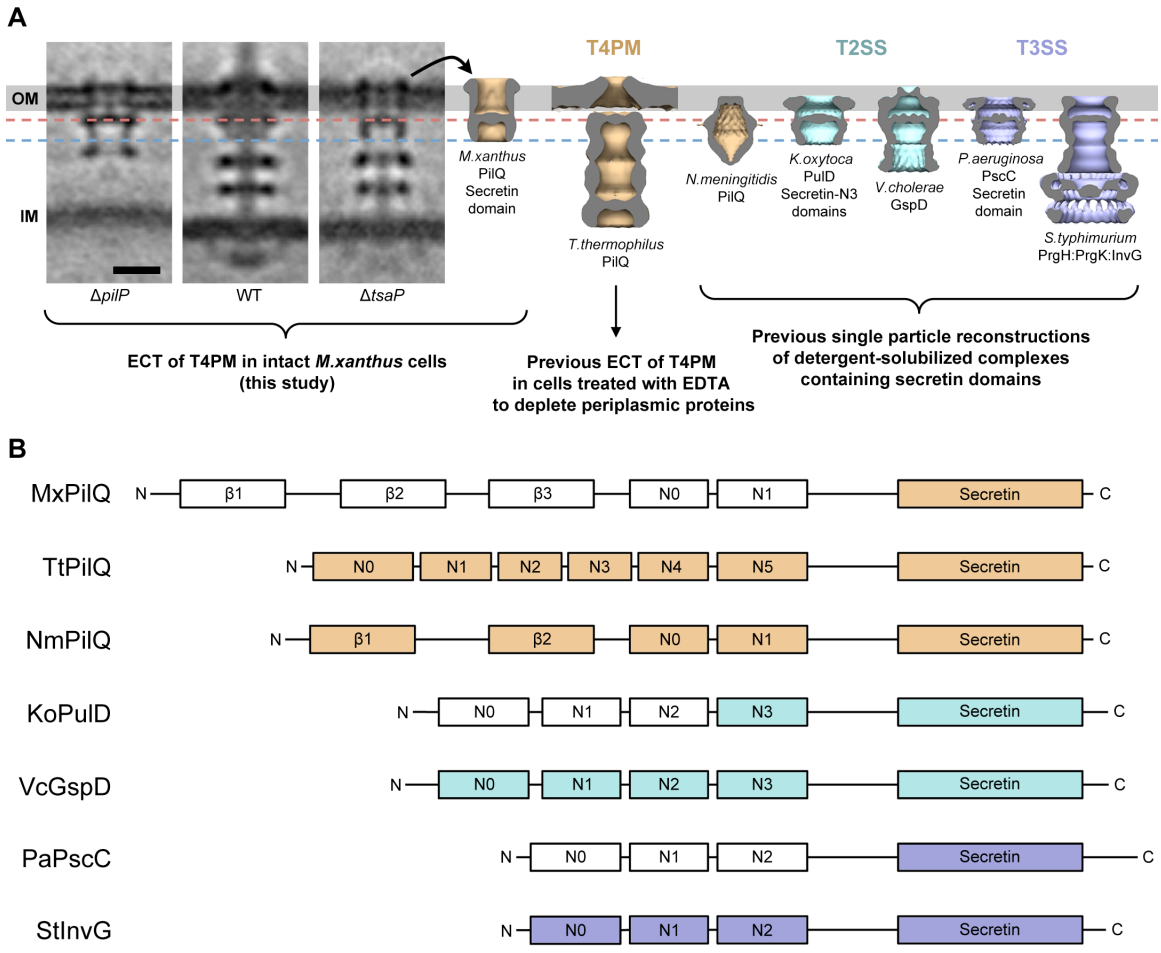

Fig. S4. PilQ structure: comparing our T4PM results with previous cryo-EM reconstructions of complexes containing secretin domains. (**A**) Sub-tomogram averages of *M. xanthus* Δ*pilP*, wild-type, and Δ*tsaP* T4PM basal bodies aligned by the OM. Arrow indicates the in vivo envelope of the PilQ secretin domain derived from the Δ*tsaP* basal body structure in this work, displayed next to a previous sub-tomogram average of *T. thermophilus* T4PM basal body (EMD 3022, only the PilQ part is shown) and single particle reconstructions of *N. meningitidis* PilQ (EMD 2105), *K. oxytoca* PulD secretin-N3 domains (EMD 2628), *V. cholerae* GspD (EMD 1763), *P. aeruginosa* PscC secretin domain (EMD 2629), and *S. typhimurium* PrgH:PrgK:InvG (EMD 1214). The single particle reconstructions are aligned to the *M. xanthus* PilQ secretin domain envelope by the conserved gate (red dashed line) and periplasmic constriction (blue dashed line), with the exception of EMD 2105, which has no clear gate and is therefore positioned based on relative location to EMD 1763 and EMD 1214 according to previous report (*41*). Scale bar 10 nm. (**B**) Schematic diagrams of the domain architecture of *M. xanthus* PilQ and the other secretin-containing proteins shown in (**A**). Only domains within the protein constructs used to generate the single particle reconstructions are colored.

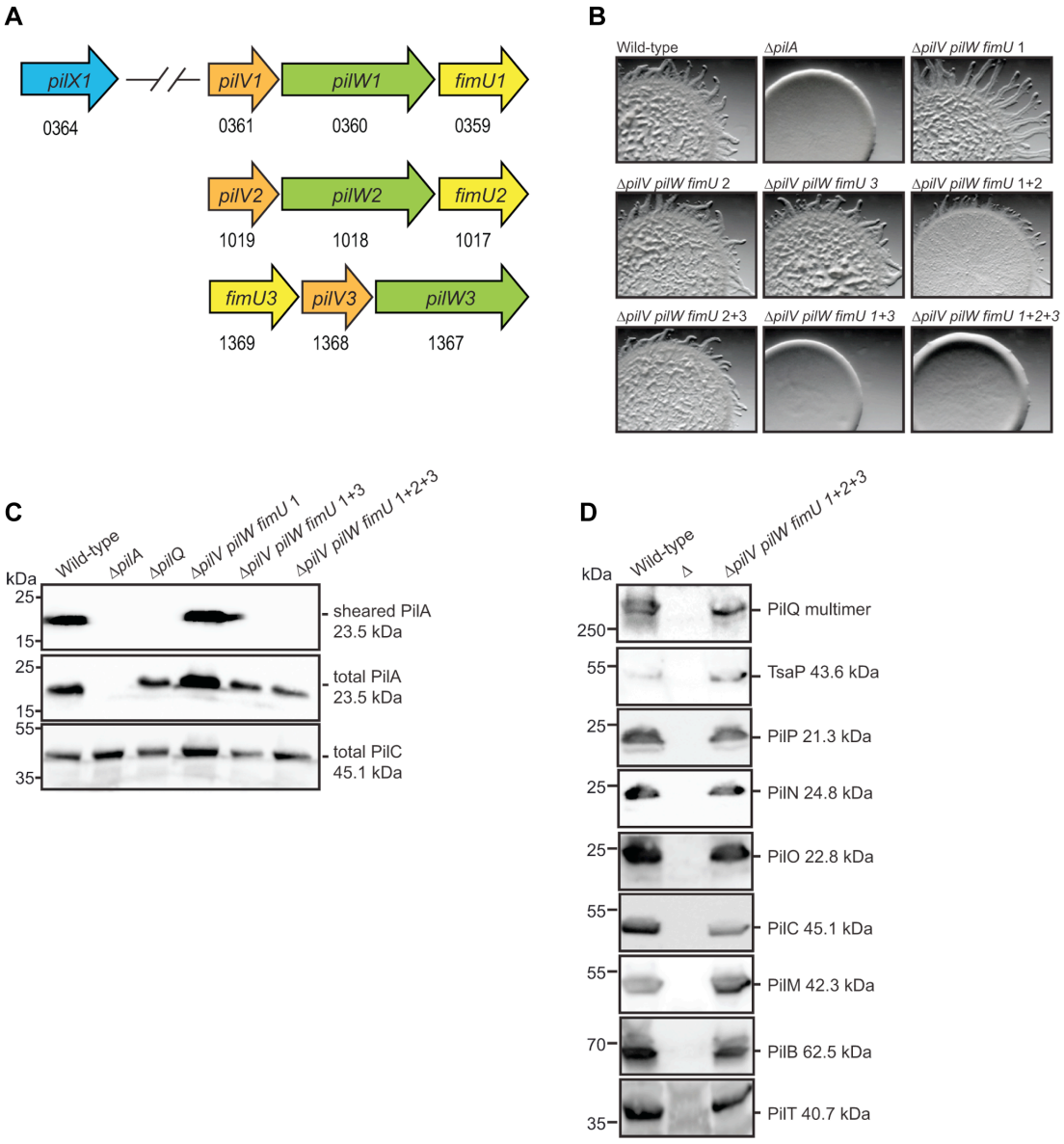

Fig. S5. *M. xanthus* T4PM minor pilins are important for T4P formation and T4P-dependent motility. (**A**) Cartoon showing the organization of minor pilin genes in the *M. xanthus* genome. The corresponding MXAN gene numbers are given below the corresponding genes. (**B**) Deletion of gene clusters for minor pilins reduces T4P-dependent motility in *M. xanthus*. *M. xanthus* strains with the indicated genotypes were incubated at 32 °C for 24 h on 0.5% agar medium supplemented with 0.5% CTT, which is favorable to T4P-dependent motility. T4P-dependent motility is scored by the formation of flares at the colony edge. Mutants deleted for *pilV pilW fimU* cluster 1 and 3 as well as for all three clusters have abolished T4P-dependent motility. (**C**) Deletion of gene clusters for minor pilins reduces T4P formation. Upper panel, T4P sheared from *M. xanthus* strains of the indicated genotypes were precipitated, then material from 15 mg of starting cells was separated by SDS-PAGE and probed with α-PilA antibodies. Middle and lower panel, total cell extract from 0.4 mg of starting cells treated as for the upper

panel was loaded per lane and first probed with α-PilA antibodies (middle panel) and after stripping probed with α-PilC antibodies (lower panel). (**D**) Deletion of gene clusters for minor pilins does not affect accumulation of T4PM proteins. Total cell extracts were isolated from exponentially growing strains of the indicated genotypes, separated by SDS-PAGE and probed with antibodies against the indicated proteins. Lanes marked Δ contain total cell extracts from the relevant deletion mutants as negative controls.

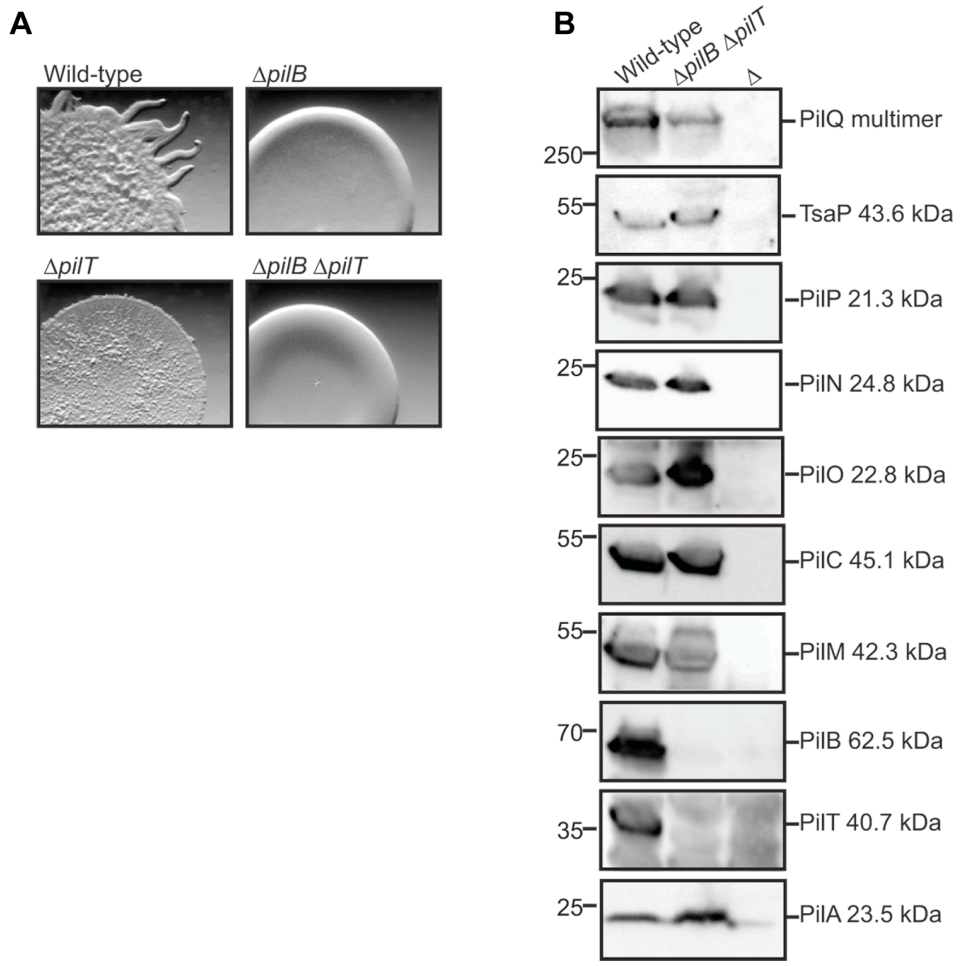

Fig. S6. A Δ*pilB* Δ*pilT* mutant lacks T4P-dependent motility but accumulates T4PM proteins. (**A**) A double deletion of *pilB* and *pilT* abolishes T4P-dependent motility. *M. xanthus* strains with the indicated genotypes were analyzed as described for Figure S5B. (**B**) A double deletion of *pilB* and *pilT* does not affect accumulation of T4PM proteins. Total cell extracts were isolated and analyzed as described in Figure S5D. Lanes marked Δ contain total cell extracts from the relevant deletion mutants as negative controls.

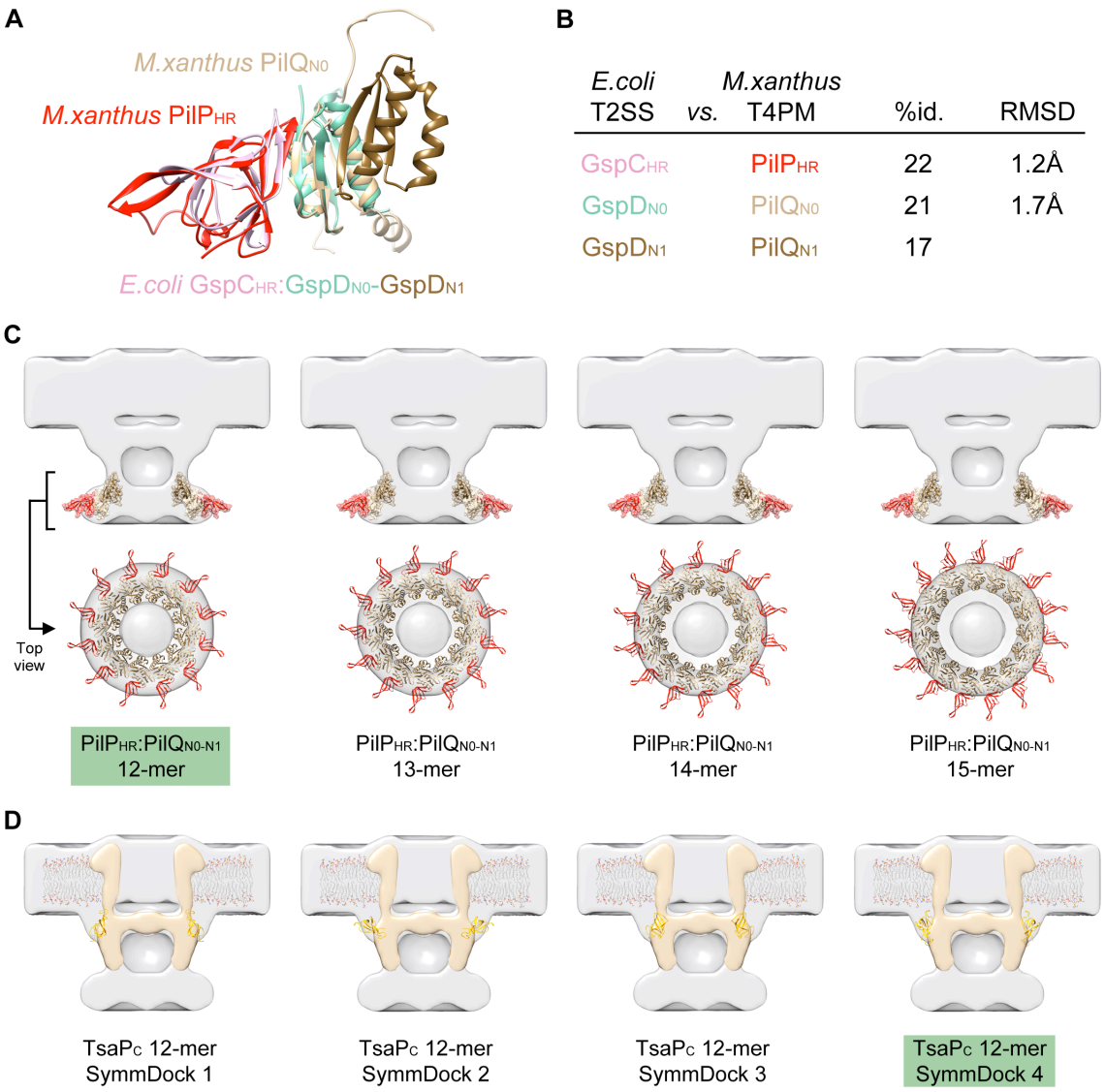

Fig. S7. Building working models of PilQ, PilP, and TsaP in the T4PM basal body. (**A**) Phyre2 models of *M. xanthus* $PilP_{HR}$ and $PilQ_{N0}$ derived from structures of T4PM homologues (Table S5) are superposed on corresponding parts in the *E. coli* T2SS $GspC_{HR}$:$GspD_{N0-N1}$ complex structure. (**B**) Percentage of amino acid sequence identity (%id.) and overall root-mean-square deviation (RMSD) between T4PM and T2SS models in (**A**). Since no structure of $PilQ_{N1}$ has been solved in T4PM homologues, the modeling of *M. xanthus* $PilQ_{N1}$ uses *E. coli* T2SS $GspD_{N1}$ as template and therefore only %id. is reported here. (**C**) SymmDock ring models containing from 12 to 15 $PilP_{HR}$:$PilQ_{N0-N1}$ complexes with $PilQ_{N1}$ (colored dark brown) on top and $PilP_{HR}$ (colored red) on the periphery, placed in the mid-periplasmic ring envelope of the empty T4PM basal body. The 12-mer $PilP_{HR}$:$PilQ_{N0-N1}$ ring fits well in the envelope while the other ring models are too large. (**D**) SymmDock ring models containing 12-mer TsaP C-terminal domains (colored yellow) with suitable diameters placed in the empty T4PM basal body envelope on the periphery of the secretin channel complex. Panels in (**C**, **D**) are sorted from left to right according to their SymmDock geometric shape complementarity score (how well

the subunits fit together around the ring) (*77*), and the rings that best matched the EM density are highlighted by green labels.

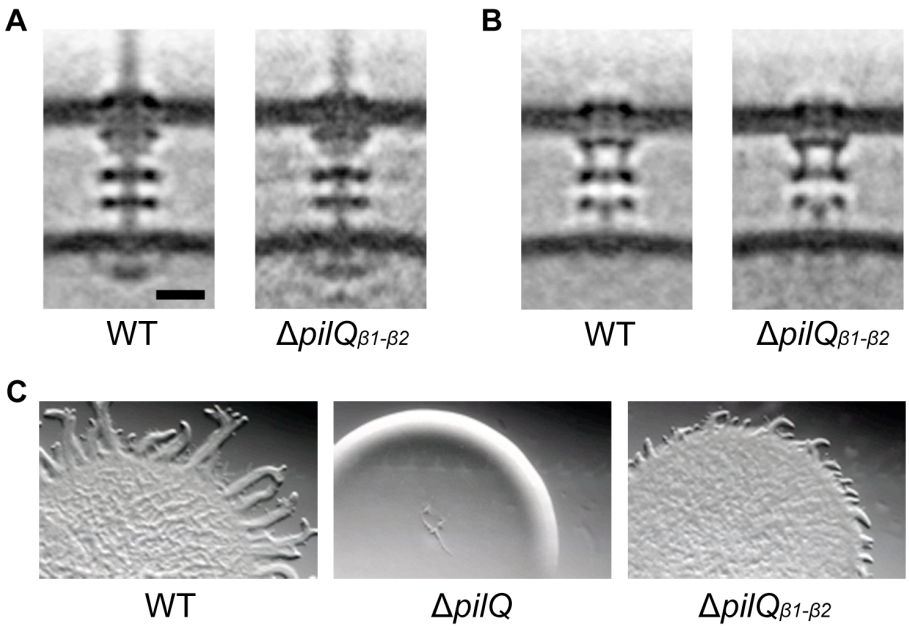

Fig. S8. Location and function of PilQ AMIN domains. (**A**, **B**) central slices of sub-tomogram averages of wild-type and Δ*pilQ*$_{β1-β2}$ T4PM basal bodies in piliated (**A**) and empty (**B**) states. (**C**) Removal of the N-terminal first two AMIN domains of PilQ reduces T4P-dependent motility. *M. xanthus* strains of the indicated genotypes were incubated at 32 °C for 24 h on 0.5% agar medium supplemented with 0.5% CTT and analyzed as described in Figure S5B.

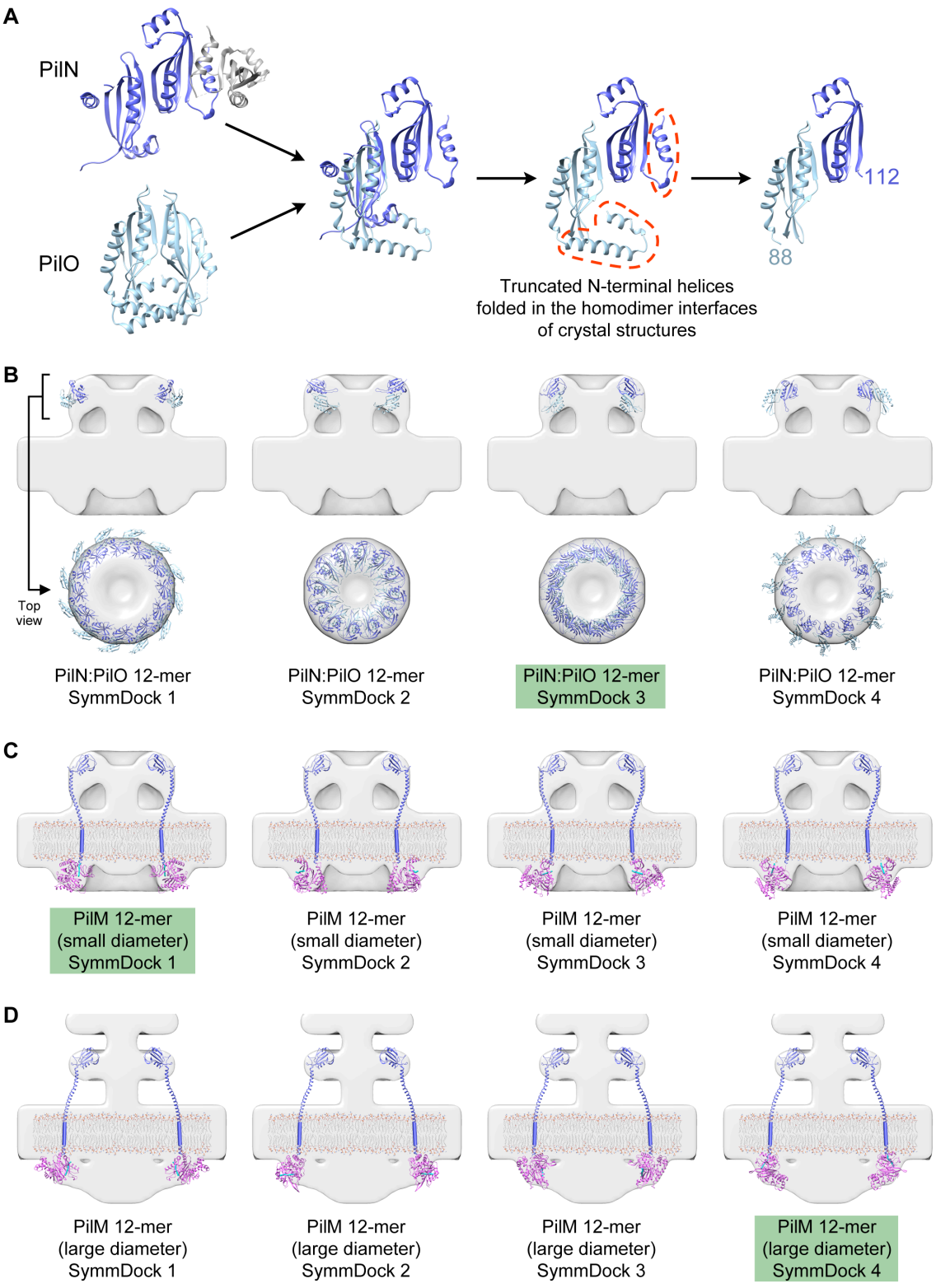

Fig. S9. Building working models of PilN, PilO, and PilM in the T4PM basal body. (**A**) The homodimeric structure of the PilN globular domain was generated by crystal packing of PDB 4BHQ (the crystal packing homodimer is colored dark blue; the other

monomer in the original crystallographic asymmetric unit is colored gray). The homodimeric structure of the PilO globular domain is PDB 2RJZ (colored light blue). To generate a heterodimer of PilN:PilO globular domains, one monomer of the PilN homodimer was replaced by a PilO monomer after being superimposed on the conserved β-sheet and α-helix. (**B**) SymmDock ring models containing 12 heterodimers of PilN and PilO globular domains and with suitable diameters placed in the lower periplasmic ring envelope of the empty T4PM basal body to inspect their fit (PilN: dark blue; PilO: light blue). (**C**) SymmDock ring models containing 12-mer PilM (colored magenta) complexed with the N-terminal peptide of PilN ($PilN_{N\text{-}terminus}$, colored cyan), with suitable diameter, placed in the cytoplasmic ring envelope of the empty basal body. Fit is assessed by both the overall shape and the feasibility of connecting $PilN_{N\text{-}terminus}$ to the PilN transmembrane segment (colored dark blue). The height of the PilN coiled-coil domain in the periplasm is defined by localization of its transmembrane segment (shown as cylinders) in the IM. (**D**) SymmDock ring models containing 12-mer PilM:$PilN_{N\text{-}terminus}$ with larger diameters than in (**C**) placed in the cytoplasmic ring envelope of the piliated T4PM basal body structure. Panels in (**B**-**D**) are sorted from left to right by SymmDock geometric shape complementarity scores with the best-fit results highlighted by green labels.

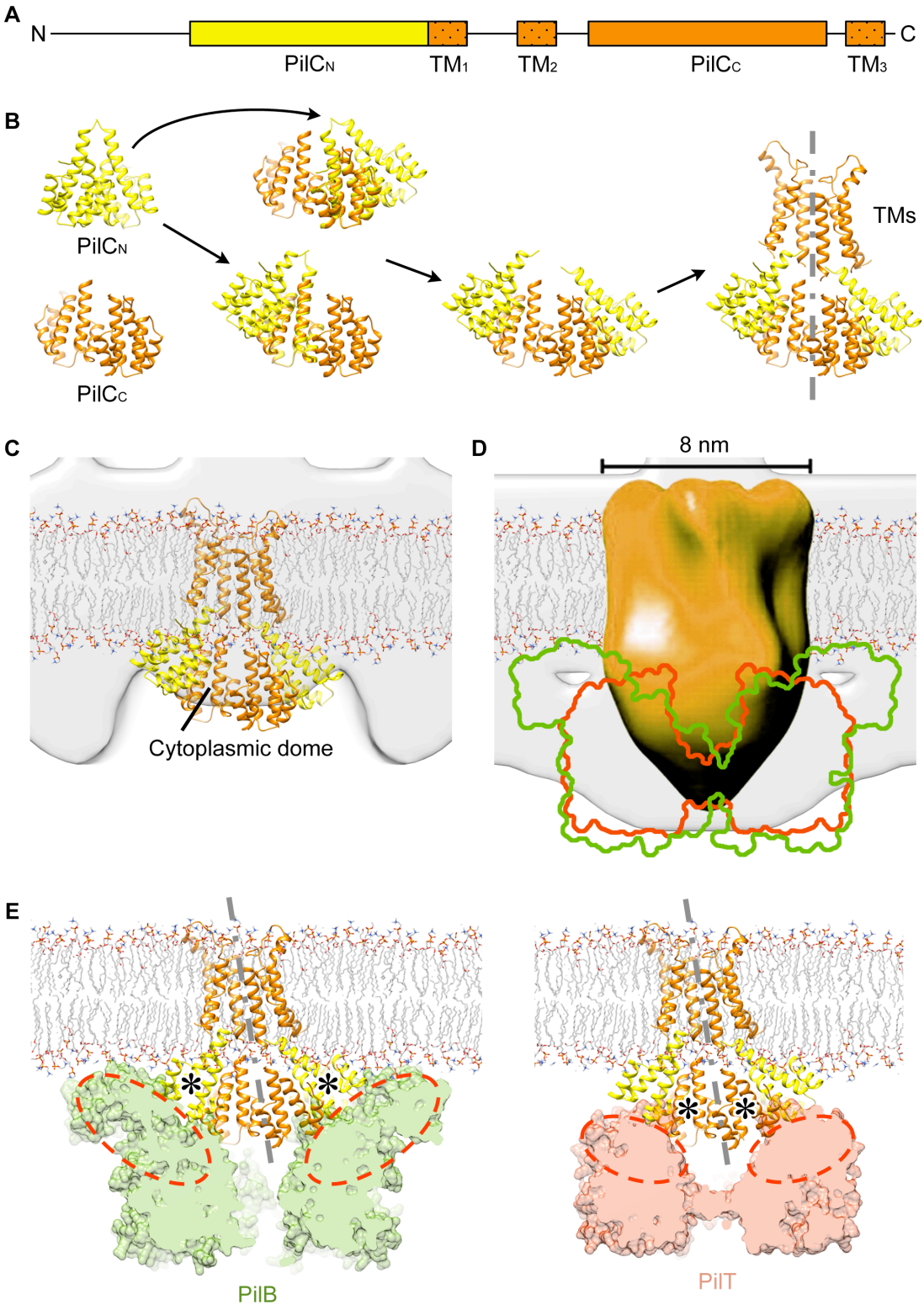

Fig. S10. Building a hypothetical working model of the PilC dimer in the T4PM basal body and its interaction with PilB and PilT ATPases. (**A**) Schematic diagram of the domain architecture of *M. xanthus* PilC. $PilC_N$: N-terminal globular domain; $PilC_C$:

C-terminal globular domain; TM: transmembrane segment. (**B**) Homodimeric models of *M. xanthus* $PilC_N$ (colored yellow) and $PilC_C$ (colored orange) were generated using PDB 3C1Q and PDB 2WHN as templates, respectively (Table S5). By superposing a $PilC_N$ homodimer onto each monomer of the $PilC_C$ homodimer and then removing the $PilC_N$ monomers used for overlay, a complex containing two $PilC_N$:$PilC_C$ was generated. The six transmembrane segments in the protein sequence of the PilC dimer were then modeled. The dimer interface of the modeled full-length PilC is indicated by the gray dashed line. The overall asymmetrical configuration is due to the asymmetrical dimer structure of PDB 2WHN, which was used to model $PilC_C$. (**C**) Fitting the PilC dimer working model generated in (**B**) into the IM and the cytoplasmic dome densities of the empty T4PM basal body envelope. (**D**) Fitting the molecular envelope of a *N. meningitidis* PilG tetramer obtained from EM single particle analysis (*90*) into the piliated T4PM basal body envelope. Image of the PilG tetramer is directly adapted from (*90*), scaled, changed color for consistency, and placed in the T4PM envelope based on its reported cytoplasmic regions. Cross-sections through the center of PilB and PilT hexamer models fitted in the cytoplasmic disc are outlined by green and red, respectively, showing clear steric clashes with the PilG tetramer. (**E**) In our model the asymmetrical PilC dimer model associates with the IM at an angle (shown by the tilted gray dashed line), allowing the two $PilC_N$ or $PilC_C$ (asterisks) in the dimer to interact with the ATPase equally. Also, the elliptical cross-section of the PilC cytoplasmic domains allows the $PilC_N$ and $PilC_C$ to interact with the wider N-terminal structure of PilB and the narrower N-terminal structure of PilT (red dashed circles), respectively, agreeing with interactions reported previously (*49*).

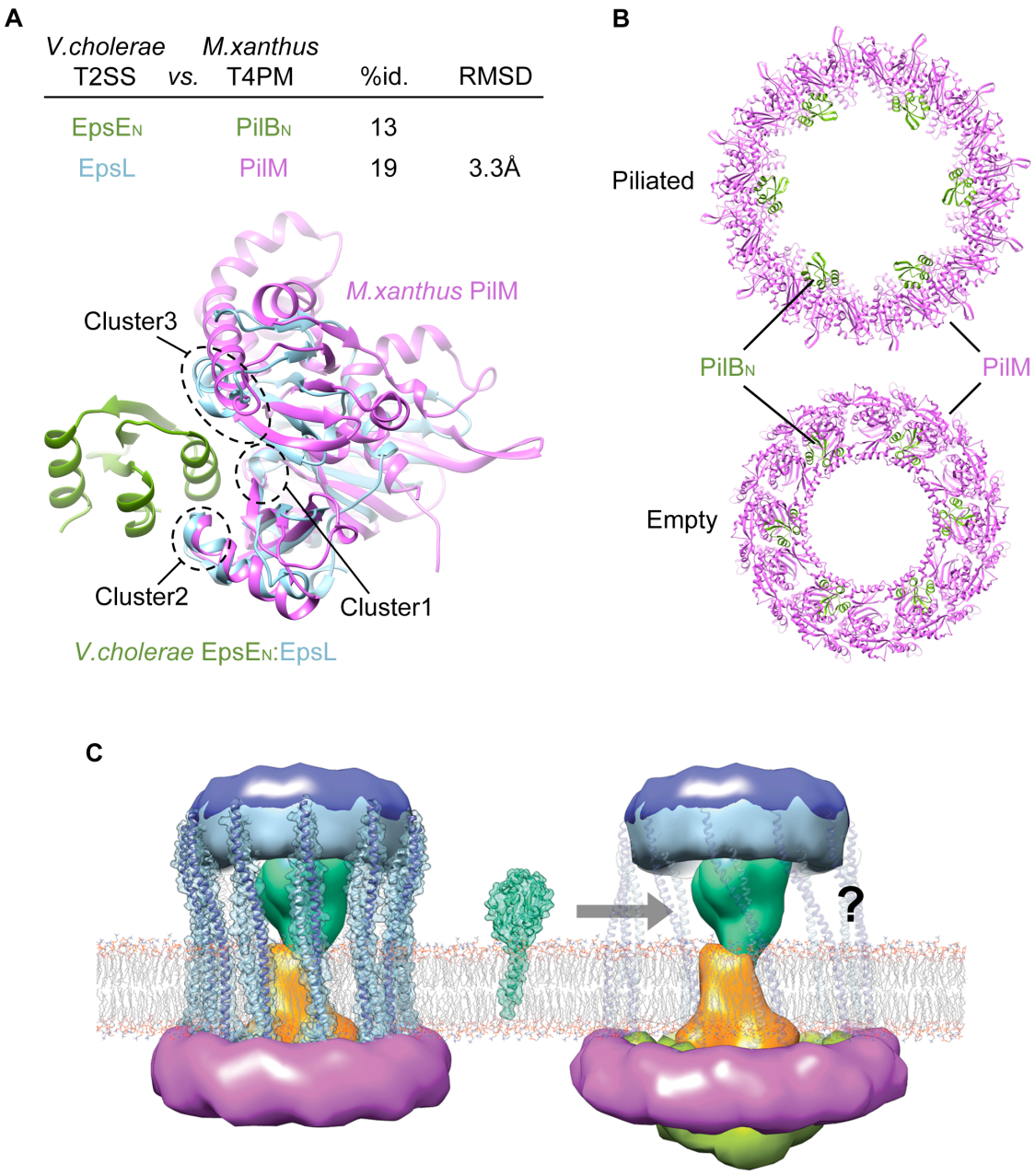

Fig. S11. ATPase-dependent PilM ring expansion and PilN:PilO cage opening. (**A**) Phyre2 model of *M. xanthus* PilM derived from the structure of *T. thermophilus* T4PM PilM is superposed on EpsL in the *V. cholerae* T2SS $EpsE_N$:EpsL complex structure. The three clusters comprising most of the interactions between $EpsE_N$ and EpsL reported previously (*36*) are marked (Cluster1-3). Percentage of amino acid sequence identity (%id.) and overall root-mean-square deviation (RMSD) between T4PM and T2SS models are reported. Since no structure of $PilB_N$ has been solved in T4PM homologues, the modeling of *M. xanthus* $PilB_N$ uses *V. cholerae* T2SS $EpsE_N$ as template and therefore only %id. is reported here. (**B**) Upper and Lower: PilM (colored magenta) 12-mer rings in piliated and empty T4PM basal body working models, respectively. Six $PilB_N$ domains (colored green) were modeled in the rings based on interactions of PilM:$PilB_N$ in (**A**).

The apparent $PilB_N$ binding sites are fully exposed on the large PilM ring in the piliated basal body model but completely buried in the small PilM ring in the empty basal body model. (**C**) Left and Right: protein surface representation of 12-mer PilM:PilN:PilO complexes extracted from the architectural models of empty and piliated T4PM basal bodies, respectively. Middle: a PilA monomer structure. Components are colored as in Figure 3B. Question mark indicates unknown conformational rearrangements of the PilN:PilO coiled-coil structures upon ATPase binding which likely modulate access of PilA.

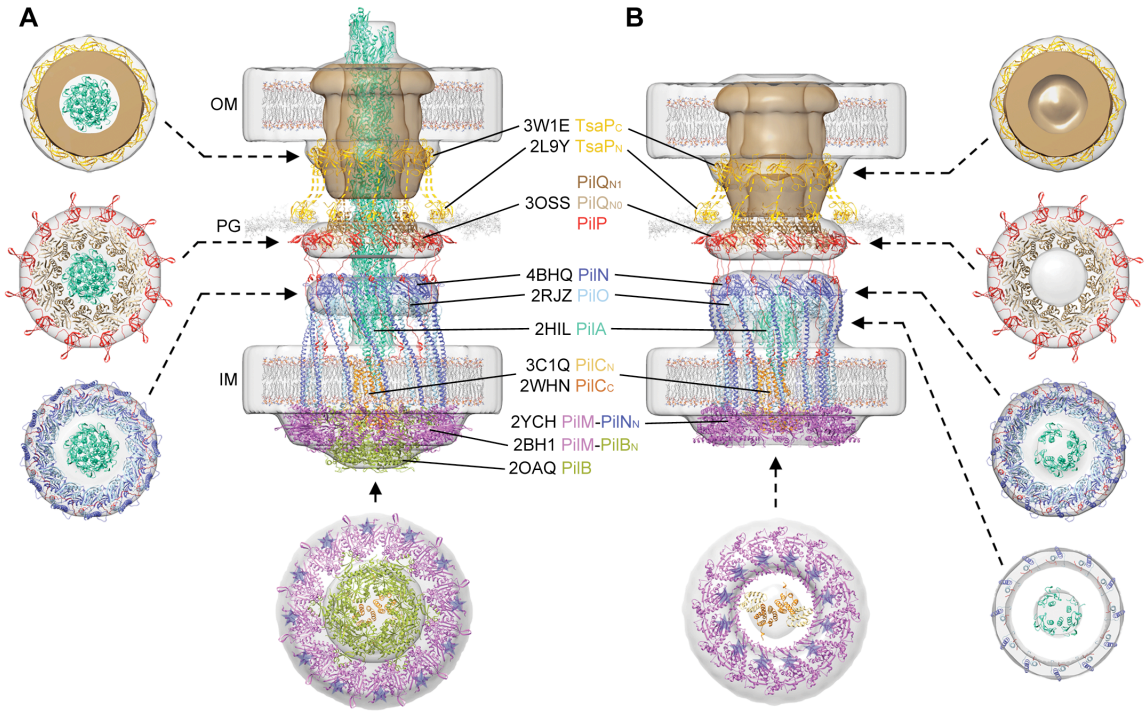

Fig. S12. Hypothetical working models of the T4PM. (**A**, **B**) Overall working models of piliated and empty T4PM basal bodies, respectively, in which atomic models of T4PM components are placed in the in vivo envelopes according to the component maps in Figure 3A and previously reported constraints. The process of placing each component is detailed in Movie 1 and Materials and Methods. Models of each component are colored corresponding to Figure 3A. Cross-sectional views of different parts of the models are indicated by arrows. For clarity, the PilQ AMIN domains, which likely bind irregularly to PG, are not shown. Blue stars on PilM rings indicate the locations of bound PilN N-termini.

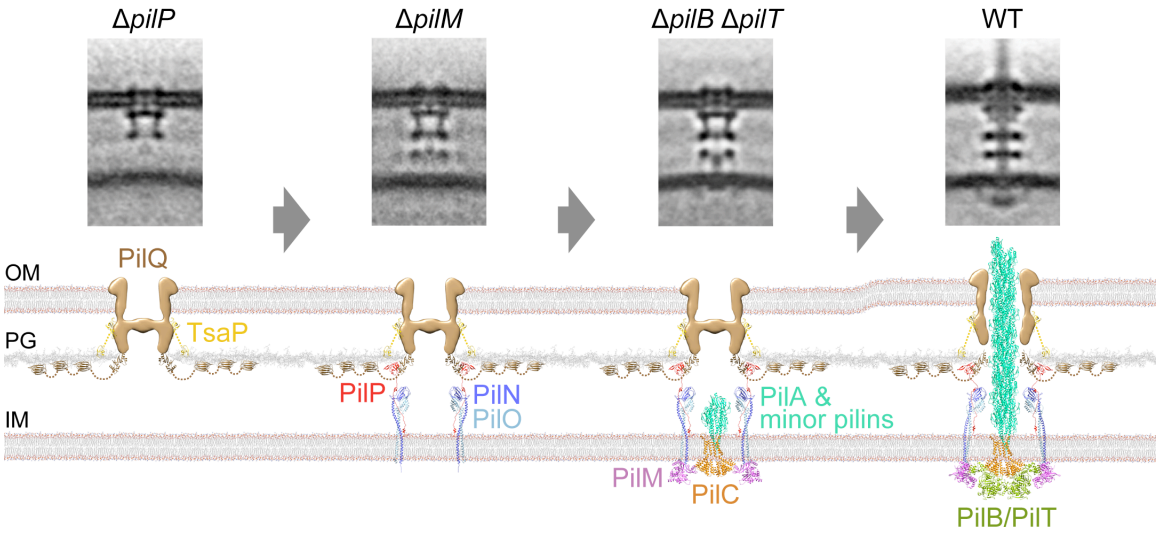

Fig. S13. Assembly pathway of the *M. xanthus* T4PM. Sub-tomogram averages (top row) and corresponding hypothetical model structures (bottom row) of assembly-competent subcomplexes likely involved in T4PM assembly in vivo. It is known from previous work that the *M. xanthus* T4PM assembles from the outside-in starting with PilQ multimer formation (*21*), and that incorporation of PilC, PilM, PilN, PilO and PilP also all require PilN, PilO, and PilP (Fig. S2), but here we show images of those basal body sub-assemblies (proving they exist) and the hypothetical models that rationalize the structural dependencies. First column: Assembly begins with polymerization of PilQ and TsaP. Noting that each PilQ monomer has multiple domains that bind to the PG, an interesting question is how would a multimeric PilQ pore-structure polymerize? One possibility is that the concentration of PilQ and TsaP monomers at the pole is so high that they can multimerize even when already tethered to the PG. Another possibility is that ring completion triggers PG binding. Second column: Anchored OM pore complexes could then become decorated by PilP complexed to PilO:PilN, eventually leading to formation of the mid-periplasmic ring and the lower periplasmic ring. Third column: Interactions between PilC and the N-terminal α-helix in the PilO that engages in formation of a coiled-coil structure with PilN (*23*) could capture a PilC dimer within the PilN:PilO coiled-coils cage before it becomes complete (a PilC dimer is likely too large to enter the cage once formed). The N-termini of PilN would further recruit PilM subunits, promoting formation of the cytoplasmic ring, which would also block movements of PilC into or out of the cage. PilC and the PilM ring then likely allow assembly of the pilins/minor pilins in the short stem. Fourth column: Finally the PilM ring would also recruit PilB, leading to pilus extension.

An alternative model is that because the *pilMNOPQ* genes form an operon in this order and are co-transcribed, perhaps the T4PM could assemble in a co-translational process (*21*). Two observations argue against this scenario, however. First, in genetic complementation experiments ectopic expression of any one of these genes leads to full complementation (*21*, *22*). Second, T4PM assembly initiates with PilQ multimer formation independently of PilM, PilN, PilO, and PilP (*21*).

The role of PilC in assembly is particularly interesting. In our model, PilC is a rotating device transferring PilA in from the IM and out to the IM. The ability of PilC to counteract the large force of T4P pulling parallel to its rotation axis while allowing PilA cargo to join or leave in orthogonal directions mimics that of an "Archimedean screw." PilC is also like a "Maxwellian demon," strategically opening and shutting a door between two compartments in opposition to entropy. In this analogy, PilC strategically biases the association or disassociation of PilA subunits onto the pilus base to drive extension and retraction. Finally, in this context it is interesting to note that archaeal flagellar motors must have transitions between growth and rotation modes that involve changes in its PilC homologue's interaction with the flagellar filament (slipping around during growth, firmly attached during rotation).

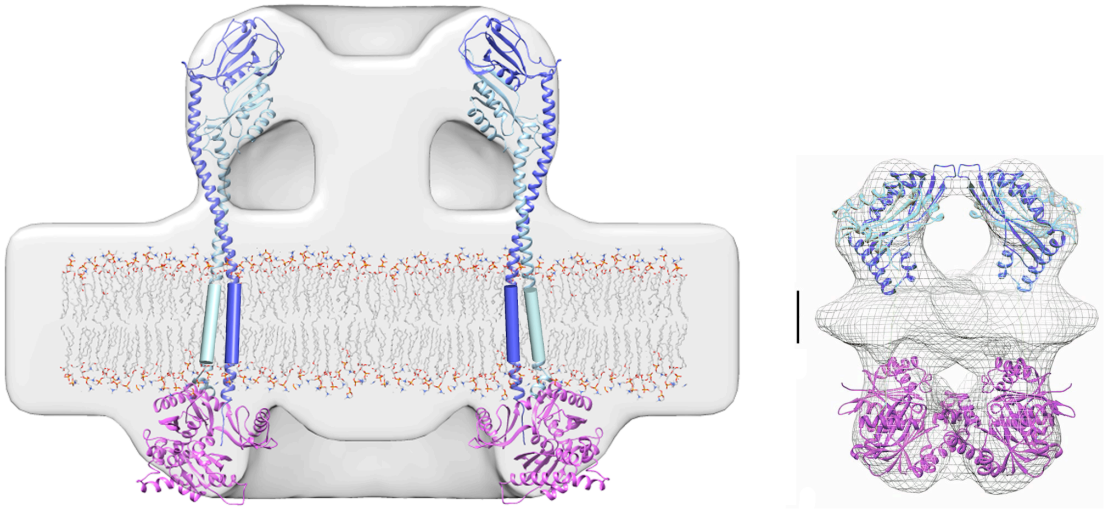

Fig. S14. Differences between PilM:PilN:PilO structural models in vivo and in vitro. Left: Our hypothetical pseudo-atomic model of a PilM:PilN:PilO complex built into the in vivo envelope of the empty T4PM basal body. Two PilM:PilN:PilO complexes spanning the cytoplasmic ring, IM, and lower periplasmic ring are shown (transmembrane segments are shown as cylinders). Right: Hypothetical pseudo-atomic model of the PilM:PilN:PilO complex previously built into a single particle reconstruction map of detergent-solubilized molecules. Image contains two copies of PilM:PilN:PilO, and is directly adapted from (*33*), with colors changed for consistency. Note that in neither case are the orientations of PilM and the globular domains of PilN and PilO certain. Secondary structures are only shown on the left for comparison to the published figure on the right.

Table S1. Number of tomograms collected and T4PM structures found on different mutants.

	WT	Δ*pilA*	Δ*pilB*	Δ*pilC*	Δ*pilM*	Δ*pilP*	Δ*pilQ*	Δ*pilT*	Δ*tsaP*
Tomograms	121	54	51	46	39	38	60	63	401
Piliated T4PM	134	0	0	0	0	0	0	159	36
Empty T4PM	93	70	230	63	72	45	0	0	42

	PilO-sfGFP	PilP-sfGFP	Δ*pilB* Δ*pilT*	Δ*pilV pilW fimU* 1+2+3	Δ$pilQ_{\beta1\text{-}\beta2}$
Tomograms	173	51	37	53	56
Piliated T4PM	50	79	0	0	41
Empty T4PM	48	80	89	80	72

Table S2. *M. xanthus* strains used in this work.

Strain name	Genotype	Reference
DK1622	wild-type	(*59*)
DK10410	Δ*pilA* (ΔMXAN5783)	(*96*)
DK10416	Δ*pilB* (ΔMXAN5788)	(*96*)
DK10417	Δ*pilC* (ΔMXAN5786)	(*96*)
SA3002	Δ*pilM* (ΔMXAN5776*)*	(*22*)
SA3004	Δ*pilN* (ΔMXAN5775)	(*21*)
SA3001	Δ*pilO* (ΔMXAN5774)	(*21*)
SA4088	Δ*pilO* /P_{pilA}-*pilO-sfGFP* (pSC106)	(*21*)
SA3005	Δ*pilP* (ΔMXAN5773)	(*21*)
SA4070	Δ*pilP* /P_{pilA}-*pilP-sfGFP* (pSC102)	(*21*)
DK10409	Δ*pilT* (ΔMXAN5787)	(*96*)
SA6011	Δ*tsaP* (ΔMXAN3001)	(*17*)
DK8615	Δ*pilQ* (ΔMXAN5772)	(*97*)
SA6808	Δ$pilQ_{\beta1\text{-}\beta2}$ (MXAN5772 Δresidues 25-300)	This study
SA6700	Δ*pilB* Δ*pilT* (ΔMXAN5788 ΔMXAN5787)	This study
SA6794	Δ*pilV pilW fimU* 1 (ΔMXAN0359-0361)	This study
SA6819	Δ*pilV pilW fimU* 2 (ΔMXAN1017-1019)	This study
SA6796	Δ*pilV pilW fimU* 3 (ΔMXAN1367-1369)	This study
SA6818	Δ*pilV pilW fimU* 1+2 (ΔMXAN0359-0361 ΔMXAN1017-1019)	This study
SA6810	Δ*pilV pilW fimU* 2+3 (ΔMXAN1017-1019 ΔMXAN1367-1369)	This study
SA6816	Δ*pilV pilW fimU* 1+3 (ΔMXAN0359-0361 ΔMXAN1367-1369)	This study
SA6815	Δ*pilV pilW fimU* 1+2+3 (ΔMXAN0359-0361 ΔMXAN1017-1019 ΔMXAN1367-1369)	This study

Table S3. Plasmids used in this work.

Plasmid	Relevant characteristics	Reference
pBJ114	*galK* containing vector for generation of in-frame deletions in *M. xanthus*, Kan^R	(*98*)
pMAT78	pBJ114 with in-frame deletion cassette for generation of an in-frame deletion of *pilT* in Δ*pilB* strain	This study
pMAT144	pBJ114 with in-frame deletion cassette for generation of an in-frame deletion of bases encoding aa25-300 in *pilQ*	This study
pMAT145	pBJ114 with in-frame deletion cassette for generation of an in-frame deletion of MXAN0361-0359	This study
pMAT146	pBJ114 with in-frame deletion cassette for generation of an in-frame deletion of MXAN1019-1017	This study
pMAT147	pBJ114 with in-frame deletion cassette for generation of an in-frame deletion of MXAN1369-1367	This study

Table S4. Primers used in this work.

Oligonucleotide	Sequence*
pilBT A	**GCGCGAATTC**GCAATCAGGAACCGTG
pilBT B	**GCGCGCTAGC**GCGAAGCTGCGGCGGAGA
pilBT C	**GCGCGCTAGC**GCGCACTCGTCCATGCAGG
pilBT D	**GCGCAAGCTT**CCTTGCCTTCGACACCGCC
pilQ A EcoRI	**GCGCGAATTC**GTCGCGATGGTCGAAGACCC
pilQ B 24 aa rev	**GGCTCTAGA**GCCCACAAGAACGACCGCCCATG
pilQ C 301 aa fwd	**GCGCTCTAGA**GCGGTTGCGCGGAAGGCTGCG
pilQ D BamHI	**GCCGGATCC**GGTGCGTGCGGAAGGACATG
mxan0361 A	**GCGCAAGCTT**CACGGGCTCTGGCATCGCCG
mxan0361 B	**GCGCTCTAGA**CGCTGTCACTGCGGCATCCT
mxan0359 C	**GCGCTCTAGA**TGAGCACTGCCGGCACCTGAAG
mxan0359 D	**GCGCGGATCC**CGGAGGTGGAGCTGCTGC
mxan1019 A	**GCGCAAGCTT**GGACTACTCGCCTGAGTCCG
mxan1019 B	**GCGCTCTAGA**CCGGTTCATGGCACCACCTC
mxan1017 C	**GCGCTCTAGA**TAGGCGGCGTCCGCACCGCC
mxan1017 D	**GCGCGAATTC**GCCGGTGGCCTGCTGCTAGC
mxan1369 A	**GCGCAAGCTT**GTTGTCCGTCAGCGCCACCG
mxan1369 B	**GCGCTCTAGA**CCGGCTCACTTGGCGACCTCC
mxan1367 C	**GCGCTCTAGA**TAGCCATCATGACCCACTTC
mxan1367 D	**GCGCGAATTC**CGCTGCCATCGAAGCGGTAG

*Primer sequences that are not complementary to the template are indicated in bold.

Table S5. Homology modeling statistics of *M. xanthus* T4PM components.

Model coverage	Model templates	%id.	Conf.
PilQ (901 residues) 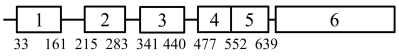	1. *E.coli* AmiC AMIN domain (4BIN) 2. *E.coli* AmiC AMIN domain (4BIN) 3. *N.meningitidis* PilQ β2 domain (4AQZ) 4. *N.meningitidis* PilQ N0 domain (4AR0) 5. *E.coli* GspD N1 domain (3OSS) 6. *M.xanthus* Δ*tsaP* basal body OM pore density	19 20 19 45 17	99.5 0.45* 99.9 99.8 99.4
TsaP (411 residues) 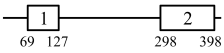	1. *M.oryzae* lectin LysM domain (2L9Y) 2. *V.alginolyticus* FlgT C-terminal domain (3W1E)	27 19	99.2 98.5
PilP (172 residues) 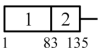	1. Manual model built based on Phyre2 server secondary structure prediction 2. *P.aeruginosa* PilP HR domain (2LC4)	 25	 100
PilN (225 residues) 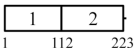	1. Manual model built based on Phyre2 server secondary structure prediction 2. *T.thermophilus* PilN C-terminal domain (4BHQ)	 22	 0.17*
PilO (205 residues) 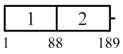	1. Manual model built based on Phyre2 server secondary structure prediction 2. *P.aeruginosa* PilO C-terminal domain (2RJZ)	 25	 99.5
PilM (395 residues) 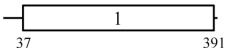	1. *T.thermophilus* PilM (2YCH)	27	100
PilA (220 residues) 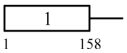	1. *N.gonorrhoeae* PilE (2HI2)	†	
PilC (417 residues) 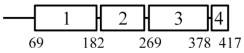	1. *V.cholerae* EpsF N-terminal domain (3C1Q) 2. Manual model built based on Phyre2 server secondary structure prediction 3. *T.thermophilus* PilC N-terminal domain (2WHN) 4. Manual model built based on Phyre server secondary structure prediction	40 25 	99.9 99.8
PilB (566 residues) 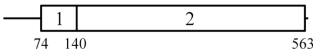	1. *V.cholerae* EpsE N-terminal domain (2BH1) 2. *A.fulgidus* GspE (2OAQ)	13 21	97.5 100
PilT (369 residues) 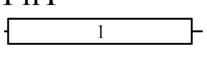	1. *P.aeruginosa* PilT (3JVV)	51	100

1st column: sequence coverage of the hypothetical working model of T4PM components. 2nd column: structural templates used for homology modeling (PDB codes are indicated in parentheses.) 3rd column: sequence identity between the template and corresponding region of the T4PM components. 4th column: confidence level from Phyre2 server. *Model is generated by SWISS-MODEL server and the global model quality estimation score is reported. †Substantial differences on protein sequence between *M. xanthus* PilA and *N. gonorrhoeae* PilE globular domains has prevented homology modeling. We therefore directly used the *N. gonorrhoeae* PilE structure in the T4PM hypothetical working model.

Movie S1. Cryo-EM tilt series of a *M. xanthus* cell pole.

Movie S2. **Cryotomogram of a *M. xanthus* cell pole capturing T4PM structures.**

Movie S3. Comparison of the T4PM conformation in piliated and empty states. Conformational differences between piliated and empty T4PMs are revealed by morphing from one density to another.

References

1. K. V. Korotkov, M. Sandkvist, W. G. J. Hol, The type II secretion system: Biogenesis, molecular architecture and mechanism. *Nat. Rev. Microbiol.* **10**, 336–351 (2012). Medline

2. K. F. Jarrell, S.-V. Albers, The archaellum: An old motility structure with a new name. *Trends Microbiol.* **20**, 307–312 (2012). Medline doi:10.1016/j.tim.2012.04.007

3. J. S. Mattick, Type IV pili and twitching motility. *Annu. Rev. Microbiol.* **56**, 289–314 (2002). Medline doi:10.1146/annurev.micro.56.012302.160938

4. L. Craig, M. E. Pique, J. A. Tainer, Type IV pilus structure and bacterial pathogenicity. *Nat. Rev. Microbiol.* **2**, 363–378 (2004). Medline doi:10.1038/nrmicro885

5. K. J. Evans, C. Lambert, R. E. Sockett, Predation by Bdellovibrio bacteriovorus HD100 requires type IV pili. *J. Bacteriol.* **189**, 4850–4859 (2007). Medline doi:10.1128/JB.01942-06

6. I. Chen, D. Dubnau, DNA uptake during bacterial transformation. *Nat. Rev. Microbiol.* **2**, 241–249 (2004). Medline doi:10.1038/nrmicro844

7. M. Klausen, A. Aaes-Jørgensen, S. Molin, T. Tolker-Nielsen, Involvement of bacterial migration in the development of complex multicellular structures in *Pseudomonas aeruginosa* biofilms. *Mol. Microbiol.* **50**, 61–68 (2003). Medline doi:10.1046/j.1365-2958.2003.03677.x

8. G. A. O'Toole, R. Kolter, Flagellar and twitching motility are necessary for *Pseudomonas aeruginosa* biofilm development. *Mol. Microbiol.* **30**, 295–304 (1998). Medline doi:10.1046/j.1365-2958.1998.01062.x

9. A. J. Hager, D. L. Bolton, M. R. Pelletier, M. J. Brittnacher, L. A. Gallagher, R. Kaul, S. J. Skerrett, S. I. Miller, T. Guina, Type IV pili-mediated secretion modulates *Francisella* virulence. *Mol. Microbiol.* **62**, 227–237 (2006). Medline doi:10.1111/j.1365-2958.2006.05365.x

10. A. J. Merz, M. So, M. P. Sheetz, Pilus retraction powers bacterial twitching motility. *Nature* **407**, 98–102 (2000). Medline doi:10.1038/35024105

11. J. M. Skerker, H. C. Berg, Direct observation of extension and retraction of type IV pili. *Proc. Natl. Acad. Sci. U.S.A.* **98**, 6901–6904 (2001). Medline doi:10.1073/pnas.121171698

12. L. Craig, J. Li, Type IV pili: Paradoxes in form and function. *Curr. Opin. Struct. Biol.* **18**, 267–277 (2008). Medline doi:10.1016/j.sbi.2007.12.009

13. P. C. Morand, E. Bille, S. Morelle, E. Eugène, J. L. Beretti, M. Wolfgang, T. F. Meyer, M. Koomey, X. Nassif, Type IV pilus retraction in pathogenic *Neisseria* is regulated by the PilC proteins. *EMBO J.* **23**, 2009–2017 (2004). Medline doi:10.1038/sj.emboj.7600200

14. B. Maier, L. Potter, M. So, C. D. Long, H. S. Seifert, M. P. Sheetz, Single pilus motor forces exceed 100 pN. *Proc. Natl. Acad. Sci. U.S.A.* **99**, 16012–16017 (2002). Medline doi:10.1073/pnas.242523299

15. M. Clausen, V. Jakovljevic, L. Søgaard-Andersen, B. Maier, High-force generation is a conserved property of type IV pilus systems. *J. Bacteriol.* **191**, 4633–4638 (2009). Medline doi:10.1128/JB.00396-09

16. V. Pelicic, Type IV pili: E pluribus unum? *Mol. Microbiol.* **68**, 827–837 (2008). Medline doi:10.1111/j.1365-2958.2008.06197.x

17. K. Siewering, S. Jain, C. Friedrich, M. T. Webber-Birungi, D. A. Semchonok, I. Binzen, A. Wagner, S. Huntley, J. Kahnt, A. Klingl, E. J. Boekema, L. Søgaard-Andersen, C. van der Does, Peptidoglycan-binding protein TsaP functions in surface assembly of type IV pili. *Proc. Natl. Acad. Sci. U.S.A.* **111**, E953–E961 (2014). Medline doi:10.1073/pnas.1322889111

18. L. Craig, N. Volkmann, A. S. Arvai, M. E. Pique, M. Yeager, E. H. Egelman, J. A. Tainer, Type IV pilus structure by cryo-electron microscopy and crystallography: Implications for pilus assembly and functions. *Mol. Cell* **23**, 651–662 (2006). Medline doi:10.1016/j.molcel.2006.07.004

19. L. L. Burrows, *Pseudomonas aeruginosa* twitching motility: Type IV pili in action. *Annu. Rev. Microbiol.* **66**, 493–520 (2012). Medline doi:10.1146/annurev-micro-092611-150055

20. J.-D. Pédelacq, S. Cabantous, T. Tran, T. C. Terwilliger, G. S. Waldo, Engineering and characterization of a superfolder green fluorescent protein. *Nat. Biotechnol.* **24**, 79–88 (2006). Medline doi:10.1038/nbt1172

21. C. Friedrich, I. Bulyha, L. Søgaard-Andersen, Outside-in assembly pathway of the type IV pilus system in *Myxococcus xanthus*. *J. Bacteriol.* **196**, 378–390 (2014). Medline doi:10.1128/JB.01094-13

22. I. Bulyha, C. Schmidt, P. Lenz, V. Jakovljevic, A. Höne, B. Maier, M. Hoppert, L. Søgaard-Andersen, Regulation of the type IV pili molecular machine by dynamic localization of two motor proteins. *Mol. Microbiol.* **74**, 691–706 (2009). Medline doi:10.1111/j.1365-2958.2009.06891.x

23. M. Georgiadou, M. Castagnini, G. Karimova, D. Ladant, V. Pelicic, Large-scale study of the interactions between proteins involved in type IV pilus biology in *Neisseria meningitidis*: Characterization of a subcomplex involved in pilus assembly. *Mol. Microbiol.* **84**, 857–873 (2012). Medline doi:10.1111/j.1365-2958.2012.08062.x

24. C. Li, R. A. Wallace, W. P. Black, Y. Z. Li, Z. Yang, Type IV pilus proteins form an integrated structure extending from the cytoplasm to the outer membrane. *PLOS ONE* **8**, e70144 (2013). Medline doi:10.1371/journal.pone.0070144

25. S. Tammam, L. M. Sampaleanu, J. Koo, K. Manoharan, M. Daubaras, L. L. Burrows, P. L. Howell, PilMNOPQ from the *Pseudomonas aeruginosa* type IV pilus system form a transenvelope protein interaction network that interacts with PilA. *J. Bacteriol.* **195**, 2126–2135 (2013). Medline doi:10.1128/JB.00032-13

26. S. V. Balasingham, R. F. Collins, R. Assalkhou, H. Homberset, S. A. Frye, J. P. Derrick, T. Tønjum, Interactions between the lipoprotein PilP and the secretin PilQ in *Neisseria meningitidis*. *J. Bacteriol.* **189**, 5716–5727 (2007). Medline doi:10.1128/JB.00060-07

27. M. Ayers, L. M. Sampaleanu, S. Tammam, J. Koo, H. Harvey, P. L. Howell, L. L. Burrows, PilM/N/O/P proteins form an inner membrane complex that affects the stability of the *Pseudomonas aeruginosa* type IV pilus secretin. *J. Mol. Biol.* **394**, 128–142 (2009). Medline doi:10.1016/j.jmb.2009.09.034

28. S. Tammam, L. M. Sampaleanu, J. Koo, P. Sundaram, M. Ayers, P. A. Chong, J. D. Forman-Kay, L. L. Burrows, P. L. Howell, Characterization of the PilN, PilO and PilP type IVa pilus subcomplex. *Mol. Microbiol.* **82**, 1496–1514 (2011). Medline doi:10.1111/j.1365-2958.2011.07903.x

29. S. Gu, G. Kelly, X. Wang, T. Frenkiel, V. E. Shevchik, R. W. Pickersgill, Solution structure of homology region (HR) domain of type II secretion system. *J. Biol. Chem.* **287**, 9072–9080 (2012). Medline doi:10.1074/jbc.M111.300624

30. L. M. Sampaleanu, J. B. Bonanno, M. Ayers, J. Koo, S. Tammam, S. K. Burley, S. C. Almo, L. L. Burrows, P. L. Howell, Periplasmic domains of *Pseudomonas aeruginosa* PilN and PilO form a stable heterodimeric complex. *J. Mol. Biol.* **394**, 143–159 (2009). Medline doi:10.1016/j.jmb.2009.09.037

31. V. Karuppiah, J. P. Derrick, Structure of the PilM-PilN inner membrane type IV pilus biogenesis complex from *Thermus thermophilus*. *J. Biol. Chem.* **286**, 24434–24442 (2011). Medline doi:10.1074/jbc.M111.243535

32. K. V. Korotkov, T. L. Johnson, M. G. Jobling, J. Pruneda, E. Pardon, A. Héroux, S. Turley, J. Steyaert, R. K. Holmes, M. Sandkvist, W. G. Hol, Structural and functional studies on the interaction of GspC and GspD in the type II secretion system. *PLOS Pathog.* **7**, e1002228 (2011). 10.1371/journal.ppat.1002228 Medline doi:10.1371/journal.ppat.1002228

33. V. Karuppiah, R. F. Collins, A. Thistlethwaite, Y. Gao, J. P. Derrick, Structure and assembly of an inner membrane platform for initiation of type IV pilus biogenesis. *Proc. Natl. Acad. Sci. U.S.A.* **110**, E4638–E4647 (2013). Medline doi:10.1073/pnas.1312313110

34. V. Karuppiah, D. Hassan, M. Saleem, J. P. Derrick, Structure and oligomerization of the PilC type IV pilus biogenesis protein from *Thermus thermophilus*. *Proteins* **78**, 2049–2057 (2010). Medline

35. J. Abendroth, D. D. Mitchell, K. V. Korotkov, T. L. Johnson, A. Kreger, M. Sandkvist, W. G. Hol, The three-dimensional structure of the cytoplasmic domains of EpsF from the type 2 secretion system of *Vibrio cholerae*. *J. Struct. Biol.* **166**, 303–315 (2009). Medline doi:10.1016/j.jsb.2009.03.009

36. J. Abendroth, P. Murphy, M. Sandkvist, M. Bagdasarian, W. G. J. Hol, The X-ray structure of the type II secretion system complex formed by the N-terminal domain of EpsE and the cytoplasmic domain of EpsL of *Vibrio cholerae*. *J. Mol. Biol.* **348**, 845–855 (2005). Medline doi:10.1016/j.jmb.2005.02.061

37. A. Yamagata, J. A. Tainer, Hexameric structures of the archaeal secretion ATPase GspE and implications for a universal secretion mechanism. *EMBO J.* **26**, 878–890 (2007). Medline doi:10.1038/sj.emboj.7601544

38. A. M. Misic, K. A. Satyshur, K. T. Forest, *P. aeruginosa* PilT structures with and without nucleotide reveal a dynamic type IV pilus retraction motor. *J. Mol. Biol.* **400**, 1011–1021 (2010). Medline doi:10.1016/j.jmb.2010.05.066

39. K. A. Satyshur, G. A. Worzalla, L. S. Meyer, E. K. Heiniger, K. G. Aukema, A. M. Misic, K. T. Forest, Crystal structures of the pilus retraction motor PilT suggest large domain movements and subunit cooperation drive motility. *Structure* **15**, 363–376 (2007). Medline doi:10.1016/j.str.2007.01.018

40. C. Lu, S. Turley, S. T. Marionni, Y. J. Park, K. K. Lee, M. Patrick, R. Shah, M. Sandkvist, M. F. Bush, W. G. Hol, Hexamers of the type II secretion ATPase GspE from *Vibrio cholerae* with increased ATPase activity. *Structure* **21**, 1707–1717 (2013). Medline doi:10.1016/j.str.2013.06.027

41. J.-L. Berry, M. M. Phelan, R. F. Collins, T. Adomavicius, T. Tønjum, S. A. Frye, L. Bird, R. Owens, R. C. Ford, L. Y. Lian, J. P. Derrick, Structure and assembly of a trans-periplasmic channel for type IV pili in *Neisseria meningitidis*. *PLOS Pathog.* **8**, e1002923 (2012). Medline doi:10.1371/journal.ppat.1002923

42. S. L. Reichow, K. V. Korotkov, W. G. J. Hol, T. Gonen, Structure of the cholera toxin secretion channel in its closed state. *Nat. Struct. Mol. Biol.* **17**, 1226–1232 (2010). Medline doi:10.1038/nsmb.1910

43. J. Kowal, M. Chami, P. Ringler, S. A. Müller, M. Kudryashev, D. Castaño-Díez, M. Amstutz, G. R. Cornelis, H. Stahlberg, A. Engel, Structure of the dodecameric *Yersinia enterocolitica* secretin YscC and its trypsin-resistant core. *Structure* **21**, 2152–2161 (2013). Medline doi:10.1016/j.str.2013.09.012

44. T. Tosi, L. F. Estrozi, V. Job, I. Guilvout, A. P. Pugsley, G. Schoehn, A. Dessen, Structural similarity of secretins from type II and type III secretion systems. *Structure* **22**, 1348–1355 (2014). 10.1016/j.str.2014.07.005 Medline doi:10.1016/j.str.2014.07.005

45. S. S. Wu, D. Kaiser, Genetic and functional evidence that Type IV pili are required for social gliding motility in *Myxococcus xanthus*. *Mol. Microbiol.* **18**, 547–558 (1995). Medline doi:10.1111/j.1365-2958.1995.mmi_18030547.x

46. Y. Nguyen, S. Sugiman-Marangos, H. Harvey, S. D. Bell, C. L. Charlton, M. S. Junop, L. L. Burrows, *Pseudomonas aeruginosa* minor pilins prime type IVa pilus assembly and promote surface display of the PilY1 adhesin. *J. Biol. Chem.* **290**, 601–611 (2015). Medline doi:10.1074/jbc.M114.616904

47. N. Sauvonnet, G. Vignon, A. P. Pugsley, P. Gounon, Pilus formation and protein secretion by the same machinery in *Escherichia coli*. *EMBO J.* **19**, 2221–2228 (2000). Medline doi:10.1093/emboj/19.10.2221

48. D. A. Cisneros, P. J. Bond, A. P. Pugsley, M. Campos, O. Francetic, Minor pseudopilin self-assembly primes type II secretion pseudopilus elongation. *EMBO J.* **31**, 1041–1053 (2012). Medline doi:10.1038/emboj.2011.454

49. H. K. Takhar, K. Kemp, M. Kim, P. L. Howell, L. L. Burrows, The platform protein is essential for type IV pilus biogenesis. *J. Biol. Chem.* **288**, 9721–9728 (2013). doi:10.1074/jbc.M113.453506

50. M. Chami, I. Guilvout, M. Gregorini, H. W. Rémigy, S. A. Müller, M. Valerio, A. Engel, A. P. Pugsley, N. Bayan, Structural insights into the secretin PulD and its trypsin-resistant core. *J. Biol. Chem.* **280**, 37732–37741 (2005). Medline doi:10.1074/jbc.M504463200

51. D. Nunn, Bacterial type II protein export and pilus biogenesis: More than just homologies? *Trends Cell Biol.* **9**, 402–408 (1999). Medline doi:10.1016/S0962-8924(99)01634-7

52. M. Clausen, M. Koomey, B. Maier, Dynamics of type IV pili is controlled by switching between multiple states. *Biophys. J.* **96**, 1169–1177 (2009). Medline doi:10.1016/j.bpj.2008.10.017

53. S.-V. Albers, K. F. Jarrell, The archaellum: How Archaea swim. *Front. Microbiol.* **6**, 23 (2015). Medline doi:10.3389/fmicb.2015.00023

54. Y. Li, H. Sun, X. Ma, A. Lu, R. Lux, D. Zusman, W. Shi, Extracellular polysaccharides mediate pilus retraction during social motility of *Myxococcus xanthus*. *Proc. Natl. Acad. Sci. U.S.A.* **100**, 5443–5448 (2003). Medline

55. N. Biais, D. L. Higashi, J. Brujić, M. So, M. P. Sheetz, Force-dependent polymorphism in type IV pili reveals hidden epitopes. *Proc. Natl. Acad. Sci. U.S.A.* **107**, 11358–11363 (2010). Medline doi:10.1073/pnas.0911328107

56. T. L. Leighton, N. Dayalani, L. M. Sampaleanu, P. L. Howell, L. L. Burrows, Novel role for PilNO in type IV pilus retraction revealed by alignment subcomplex mutations. *J. Bacteriol.* **197**, 2229–2238 (2015). doi:10.1128/JB.00220-15

57. S. Chen, M. Beeby, G. E. Murphy, J. R. Leadbetter, D. R. Hendrixson, A. Briegel, Z. Li, J. Shi, E. I. Tocheva, A. Müller, M. J. Dobro, G. J. Jensen, Structural diversity of bacterial flagellar motors. *EMBO J.* **30**, 2972–2981 (2011). Medline doi:10.1038/emboj.2011.186

58. A. Briegel, M. L. Wong, H. L. Hodges, C. M. Oikonomou, K. N. Piasta, M. J. Harris, D. J. Fowler, L. K. Thompson, J. J. Falke, L. L. Kiessling, G. J. Jensen, New insights into bacterial chemoreceptor array structure and assembly from electron cryotomography. *Biochemistry* **53**, 1575–1585 (2014). doi:10.1021/bi5000614

59. D. Kaiser, Social gliding is correlated with the presence of pili in *Myxococcus xanthus*. *Proc. Natl. Acad. Sci. U.S.A.* **76**, 5952–5956 (1979). Medline doi:10.1073/pnas.76.11.5952

60. L. Søgaard-Andersen, F. J. Slack, H. Kimsey, D. Kaiser, Intercellular C-signaling in *Myxococcus xanthus* involves a branched signal transduction pathway. *Genes Dev.* **10**, 740–754 (1996). Medline doi:10.1101/gad.10.6.740

61. X. Shi, S. Wegener-Feldbrügge, S. Huntley, N. Hamann, R. Hedderich, L. Søgaard-Andersen, Bioinformatics and experimental analysis of proteins of two-component systems in *Myxococcus xanthus*. *J. Bacteriol.* **190**, 613–624 (2008). Medline doi:10.1128/JB.01502-07

62. W. Shi, D. R. Zusman, The two motility systems of *Myxococcus xanthus* show different selective advantages on various surfaces. *Proc. Natl. Acad. Sci. U.S.A.* **90**, 3378–3382 (1993). Medline doi:10.1073/pnas.90.8.3378

63. Y. Li, R. Lux, A. E. Pelling, J. K. Gimzewski, W. Shi, Analysis of type IV pilus and its associated motility in *Myxococcus xanthus* using an antibody reactive with native pilin and pili. *Microbiology* **151**, 353–360 (2005). Medline doi:10.1099/mic.0.27614-0

64. V. Jakovljevic, S. Leonardy, M. Hoppert, L. Søgaard-Andersen, PilB and PilT are ATPases acting antagonistically in type IV pilus function in *Myxococcus xanthus*. *J. Bacteriol.* **190**, 2411–2421 (2008). Medline doi:10.1128/JB.01793-07

65. S. S. Wu, D. Kaiser, Regulation of expression of the pilA gene in *Myxococcus xanthus*. *J. Bacteriol.* **179**, 7748–7758 (1997). Medline

66. M. Y. Galperin, K. S. Makarova, Y. I. Wolf, E. V. Koonin, Expanded microbial genome coverage and improved protein family annotation in the COG database. *Nucleic Acids Res.* **43**, D261–D269 (2015). Medline doi:10.1093/nar/gku1223

67. A. Konovalova, T. Petters, L. Søgaard-Andersen, Extracellular biology of *Myxococcus xanthus*. *FEMS Microbiol. Rev.* **34**, 89–106 (2010). Medline doi:10.1111/j.1574-6976.2009.00194.x

68. S. Q. Zheng, B. Keszthelyi, E. Branlund, J. M. Lyle, M. B. Braunfeld, J. W. Sedat, D. A. Agard, UCSF tomography: An integrated software suite for real-time electron microscopic tomographic data collection, alignment, and reconstruction. *J. Struct. Biol.* **157**, 138–147 (2007). Medline doi:10.1016/j.jsb.2006.06.005

69. J. R. Kremer, D. N. Mastronarde, J. R. McIntosh, Computer visualization of three-dimensional image data using IMOD. *J. Struct. Biol.* **116**, 71–76 (1996). Medline doi:10.1006/jsbi.1996.0013

70. J. I. Agulleiro, J. J. Fernandez, Fast tomographic reconstruction on multicore computers. *Bioinformatics* **27**, 582–583 (2011). Medline doi:10.1093/bioinformatics/btq692

71. D. Nicastro, C. Schwartz, J. Pierson, R. Gaudette, M. E. Porter, J. R. McIntosh, The molecular architecture of axonemes revealed by cryoelectron tomography. *Science* **313**, 944–948 (2006). Medline doi:10.1126/science.1128618

72. T. Mignot, J. P. Merlie Jr., D. R. Zusman, Regulated pole-to-pole oscillations of a bacterial gliding motility protein. *Science* **310**, 855–857 (2005). Medline doi:10.1126/science.1119052

73. M. Kudryashev, M. Stenta, S. Schmelz, M. Amstutz, U. Wiesand, D. Castaño-Díez, M. T. Degiacomi, S. Münnich, C. K. Bleck, J. Kowal, A. Diepold, D. W. Heinz, M. Dal Peraro, G. R. Cornelis, H. Stahlberg, In situ structural analysis of the *Yersinia enterocolitica* injectisome. *eLife* **2**, e00792 (2013). Medline doi:10.7554/eLife.00792

74. L. A. Kelley, S. Mezulis, C. M. Yates, M. N. Wass, M. J. E. Sternberg, The Phyre2 web portal for protein modeling, prediction and analysis. *Nat. Protoc.* **10**, 845–858 (2015). Medline doi:10.1038/nprot.2015.053

75. O. Schraidt, T. C. Marlovits, Three-dimensional model of *Salmonella*'s needle complex at subnanometer resolution. *Science* **331**, 1192–1195 (2011). Medline doi:10.1126/science.1199358

76. N. Opalka, R. Beckmann, N. Boisset, M. N. Simon, M. Russel, S. A. Darst, Structure of the filamentous phage pIV multimer by cryo-electron microscopy. *J. Mol. Biol.* **325**, 461–470 (2003). Medline doi:10.1016/S0022-2836(02)01246-9

77. D. Schneidman-Duhovny, Y. Inbar, R. Nussinov, H. J. Wolfson, PatchDock and SymmDock: Servers for rigid and symmetric docking. *Nucleic Acids Res.* **33**, W363–W367 (2005). Medline doi:10.1093/nar/gki481

78. M. Rocaboy, R. Herman, E. Sauvage, H. Remaut, K. Moonens, M. Terrak, P. Charlier, F. Kerff, The crystal structure of the cell division amidase AmiC reveals the fold of the AMIN domain, a new peptidoglycan binding domain. *Mol. Microbiol.* **90**, 267–277 (2013). Medline

79. J. Koo, T. Tang, H. Harvey, S. Tammam, L. Sampaleanu, L. L. Burrows, P. L. Howell, Functional mapping of PilF and PilQ in the *Pseudomonas aeruginosa* type IV pilus system. *Biochemistry* **52**, 2914–2923 (2013). Medline doi:10.1021/bi3015345

80. R. M. Martinez, B. A. Jude, T. J. Kirn, K. Skorupski, R. K. Taylor, Role of FlgT in anchoring the flagellum of *Vibrio cholerae*. *J. Bacteriol.* **192**, 2085–2092 (2010). Medline doi:10.1128/JB.01562-09

81. H. Terashima, M. Koike, S. Kojima, M. Homma, The flagellar basal body-associated protein FlgT is essential for a novel ring structure in the sodium-driven *Vibrio* motor. *J. Bacteriol.* **192**, 5609–5615 (2010). Medline doi:10.1128/JB.00720-10

82. L. M. I. Koharudin, A. R. Viscomi, B. Montanini, M. J. Kershaw, N. J. Talbot, S. Ottonello, A. M. Gronenborn, Structure-function analysis of a CVNH-LysM lectin expressed during plant infection by the rice blast fungus *Magnaporthe oryzae*. *Structure* **19**, 662–674 (2011). Medline doi:10.1016/j.str.2011.03.004

83. H. Terashima, N. Li, M. Sakuma, M. Koike, S. Kojima, M. Homma, K. Imada, Insight into the assembly mechanism in the supramolecular rings of the sodium-driven *Vibrio* flagellar motor from the structure of FlgT. *Proc. Natl. Acad. Sci. U.S.A.* **110**, 6133–6138 (2013). Medline doi:10.1073/pnas.1222655110

84. M. Lallemand, F. H. Login, N. Guschinskaya, C. Pineau, G. Effantin, X. Robert, V. E. Shevchik, Dynamic interplay between the periplasmic and transmembrane domains of GspL and GspM in the type II secretion system. *PLOS ONE* **8**, e79562 (2013). Medline doi:10.1371/journal.pone.0079562

85. K. V. Korotkov, W. G. J. Hol, Structure of the GspK-GspI-GspJ complex from the enterotoxigenic *Escherichia coli* type 2 secretion system. *Nat. Struct. Mol. Biol.* **15**, 462–468 (2008). Medline doi:10.1038/nsmb.1426

86. J. D. Thomas, P. J. Reeves, G. P. C. Salmond, The general secretion pathway of *Erwinia carotovora* subsp. *carotovora*: Analysis of the membrane topology of OutC and OutF. *Microbiology* **143**, 713–720 (1997). Medline doi:10.1099/00221287-143-3-713

87. J. Arts, A. de Groot, G. Ball, E. Durand, M. El Khattabi, A. Filloux, J. Tommassen, M. Koster, Interaction domains in the *Pseudomonas aeruginosa* type II secretory apparatus component XcpS (GspF). *Microbiology* **153**, 1582–1592 (2007). Medline doi:10.1099/mic.0.2006/002840-0

88. T. E. Blank, M. S. Donnenberg, Novel topology of BfpE, a cytoplasmic membrane protein required for type IV fimbrial biogenesis in enteropathogenic *Escherichia coli*. *J. Bacteriol.* **183**, 4435–4450 (2001). Medline doi:10.1128/JB.183.15.4435-4450.2001

89. S. Kolappan, L. Craig, Structure of the cytoplasmic domain of TcpE, the inner membrane core protein required for assembly of the *Vibrio cholerae* toxin-coregulated pilus. *Acta Crystallogr. D* **69**, 513–519 (2013). Medline doi:10.1107/S0907444912050330

90. R. F. Collins, M. Saleem, J. P. Derrick, Purification and three-dimensional electron microscopy structure of the *Neisseria meningitidis* type IV pilus biogenesis protein PilG. *J. Bacteriol.* **189**, 6389–6396 (2007). Medline doi:10.1128/JB.00648-07

91. P. Chiang, M. Habash, L. L. Burrows, Disparate subcellular localization patterns of *Pseudomonas aeruginosa* Type IV pilus ATPases involved in twitching motility. *J. Bacteriol.* **187**, 829–839 (2005). Medline doi:10.1128/JB.187.3.829-839.2005

92. A. Kucukelbir, F. J. Sigworth, H. D. Tagare, Quantifying the local resolution of cryo-EM density maps. *Nat. Methods* **11**, 63–65 (2014). Medline doi:10.1038/nmeth.2727

93. I. Bulyha, S. Lindow, L. Lin, K. Bolte, K. Wuichet, J. Kahnt, C. van der Does, M. Thanbichler, L. Søgaard-Andersen, Two small GTPases act in concert with the bactofilin cytoskeleton to regulate dynamic bacterial cell polarity. *Dev. Cell* **25**, 119–131 (2013). Medline doi:10.1016/j.devcel.2013.02.017

94. S. Leonardy, M. Miertzschke, I. Bulyha, E. Sperling, A. Wittinghofer, L. Søgaard-Andersen, Regulation of dynamic polarity switching in bacteria by a Ras-like G-protein and its cognate GAP. *EMBO J.* **29**, 2276–2289 (2010). Medline doi:10.1038/emboj.2010.114

95. E. Nudleman, D. Wall, D. Kaiser, Polar assembly of the type IV pilus secretin in *Myxococcus xanthus*. *Mol. Microbiol.* **60**, 16–29 (2006). Medline doi:10.1111/j.1365-2958.2006.05095.x

96. S. S. Wu, J. Wu, D. Kaiser, The *Myxococcus xanthus* pilT locus is required for social gliding motility although pili are still produced. *Mol. Microbiol.* **23**, 109–121 (1997). Medline doi:10.1046/j.1365-2958.1997.1791550.x

97. D. Wall, P. E. Kolenbrander, D. Kaiser, The *Myxococcus xanthus* pilQ (sglA) gene encodes a secretin homolog required for type IV pilus biogenesis, social motility, and development. *J. Bacteriol.* **181**, 24–33 (1999). Medline

98. B. Julien, A. D. Kaiser, A. Garza, Spatial control of cell differentiation in *Myxococcus xanthus*. *Proc. Natl. Acad. Sci. U.S.A.* **97**, 9098–9103 (2000). Medline doi:10.1073/pnas.97.16.9098